PERGAMON

International Journal of Solids and Structures 40 (2003) 3967–4001

INTERNATIONAL JOURNAL OF SOLIDS and STRUCTURES

www.elsevier.com/locate/ijsolstr

The interaction integral for fracture of orthotropic functionally graded materials: evaluation of stress intensity factors

Jeong-Ho Kim, Glaucio H. Paulino *

Department of Civil and Environmental Engineering, University of Illinois at Urbana-Champaign, Newmark Laboratory, 205 North Mathews Avenue, Urbana, IL 61801, USA

Received 26 July 2002; received in revised form 11 March 2003

Abstract

The interaction integral is an accurate and robust scheme for evaluating mixed-mode stress intensity factors. This paper extends the concept to orthotropic functionally graded materials and addresses fracture mechanics problems with arbitrarily oriented straight and/or curved cracks. The gradation of orthotropic material properties are smooth functions of spatial coordinates, which are integrated into the element stiffness matrix using the so-called "generalized isoparametric formulation". The types of orthotropic material gradation considered include exponential, radial, and hyperbolic-tangent functions. Stress intensity factors for mode I and mixed-mode two-dimensional problems are evaluated by means of the interaction integral and the finite element method. Extensive computational experiments have been performed to validate the proposed formulation. The accuracy of numerical results is discussed by comparison with available analytical, semi-analytical, or numerical solutions.

Keywords: Functionally graded material (FGM); Fracture mechanics; Stress intensity factor (SIF); Interaction integral; Finite element method (FEM); Generalized isoparametric formulation (GIF)

1. Introduction

Functionally graded materials (FGMs) are a new class of composites in which the volume fraction of constituent materials vary smoothly, giving a nonuniform microstructure with continuously graded macroproperties (Hirai, 1993; Paulino et al., 2002). These multifunctional materials were introduced to take advantage of ideal behavior of its constituents, e.g. heat and corrosion resistance of ceramics together with mechanical strength and toughness of metals. In practice, the nature of processing techniques of some FGMs may lead to loss of isotropy. For example, graded materials processed by a *plasma spray* technique generally have a lamellar structure (Sampath et al., 1995) (see Fig. 1(a)), where flattened splats and

* Corresponding author. Tel.: +1-217-333-3817; fax: +1-217-265-8041.
E-mail address: paulino@uiuc.edu (G.H. Paulino).

0020-7683/03/$ - see front matter © 2003 Elsevier Science Ltd. All rights reserved.
doi:10.1016/S0020-7683(03)00176-8

Nomenclature

a	half crack length
a_{ij}	contracted notation of the compliance tensor for plane stress; $i,j=1,2,\ldots,6$
a_{ij}^{tip}	a_{ij} evaluated at the crack tip location; $i,j=1,2,\ldots,6$
b_{ij}	contracted notation of the compliance tensor for plane strain; $i,j=1,2,\ldots,6$
c_{11}, c_{22}, c_{12}	coefficients in the relationship between J and stress intensity factors (K_{I} and K_{II})
C_{ijkl} or $\mathbf{C}$	constitutive tensor for anisotropic materials; $i,j,k,l=1,2,3$
d	translation factor in the hyperbolic-tangent function
e	natural logarithm base, $\text{e}=2.71828182\ldots$
E	effective Young's modulus in orthotropic materials; $E=\sqrt{E_{11}E_{22}}$
E^0	effective Young's modulus evaluated at the origin; $E^0=\sqrt{E_{11}^0E_{22}^0}$
E_{11}, E_{22}	Young's moduli with respect to the principal axes of orthotropy
E_{11}^0, E_{22}^0	Young's moduli E_{11}, E_{22} evaluated at the origin
G_{12}	shear modulus in orthotropic materials
$\mathscr{G}_{\text{I}}$	mode I energy release rate
$\mathscr{G}_{\text{II}}$	mode II energy release rate
h_1, h_2	dimensions of the beam specimen
H	length of material gradation
$\mathscr{H}$	contour integral
Im	imaginary part of the complex function
J	path-independent J-integral for the actual field
J^{aux}	J-integral for the auxiliary field
J^{s}	J-integral for the superimposed fields (actual and auxiliary)
$\mathbf{J}$	Jacobian matrix
$\mathbf{J}^{-1}$	inverse of the Jacobian matrix
K_{I}	mode I stress intensity factor
K_{II}	mode II stress intensity factor
K_0	normalizing factor for stress intensity factors, $K_0=\varepsilon_0\overline{E}^0\sqrt{\pi a}$, $\overline{E}^0=E^0/\delta^2$
$\lvert K\rvert$	norm of stress intensity factors, $\lvert K\rvert=\sqrt{K_{\text{I}}^2+K_{\text{II}}^2}$
L	length of a plate
M	interaction integral (M-integral)
m_i, n_i	unit normal vectors on the contour of the domain integral
p_k, q_k	coefficients of the asymptotic displacements for orthotropic materials; $k=1,2$
q	weight function in the domain integral
r	radial direction in polar coordinates
Re	real part of the complex function
S_{ijkl} or $\mathbf{S}$	compliance tensor for anisotropic materials; $i,j,k,l=1,2,3$
u_i	displacements for the actual field; $i=1,2$
u_i^{aux}	displacements for the auxiliary field; $i=1,2$
W	width of a plate
$\mathscr{W}$	strain energy density
$\mathscr{W}^{\text{aux}}$	strain energy density for the auxiliary field
x_i	local Cartesian coordinates; $i=1,2$
X_i	global Cartesian coordinates; $i=1,2$
z_k	complex variable, $z_k=x_k+\text{i}y_k$; $k=1,2$

α	material nonhomogeneity parameter for gradation of E_{11}
α_k	the real part of μ_k; $k = 1, 2$
β	material nonhomogeneity parameter for gradation of E_{22}
β_k	the imaginary part of μ_k; $k = 1, 2$
γ	material nonhomogeneity parameter for gradation of G_{12}
Γ	contour for J and M integrals
Γ_0	outer contour
Γ_s	inner contour
Γ^+	contour along the upper crack face
Γ^-	contour along the lower crack face
δ^4	stiffness ratio, $\delta^4 = E_{11}/E_{22} = \nu_{12}/\nu_{21}$
δ_{ij}	Kronecker delta; $i, j = 1, 2$
ε_k	contracted notation of ε_{ij}; $k = 1, \ldots, 6$
ε_{ij}	strains for the actual fields; $i, j = 1, 2, 3$
$\varepsilon_{ij}^{\text{aux}}$	strains for the auxiliary fields; $i, j = 1, 2, 3$
θ	angular direction in polar coordinates
κ_0	shear parameter, $\kappa_0 = E/(2G_{12}) - \nu$
μ_k	roots of the characteristic equation; $k = 1, 2$
μ_k^{tip}	μ_k evaluated at the crack tip location; $k = 1, 2$
$\overline{\mu}_k$	complex conjugate of μ_k; $k = 1, 2$
ν	effective Poisson's ratio, $\nu = \sqrt{\nu_{12}\nu_{21}}$
ν_{ij}	Poisson's ratio representing the response in direction j due to loading in direction i
σ_k	contracted notation of σ_{ij}; $k = 1, \ldots, 6$
σ_{ij}	stresses for the actual fields; $i, j = 1, 2, 3$
σ_{ij}^{aux}	stresses for the auxiliary fields; $i, j = 1, 2, 3$

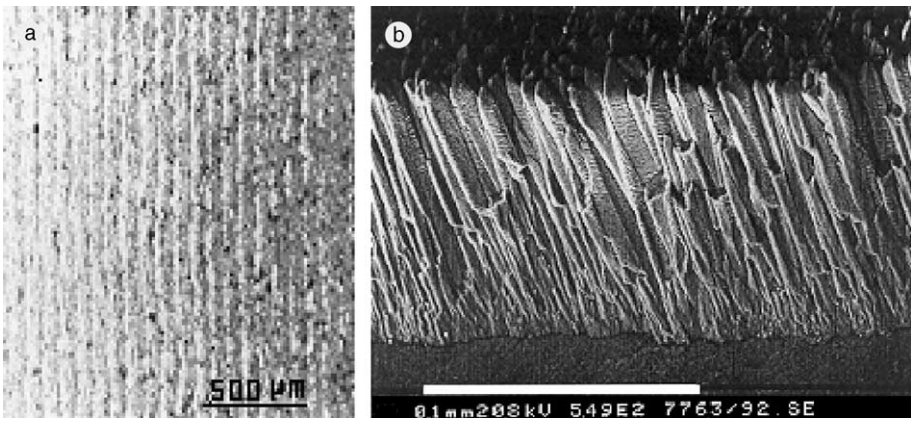

Fig. 1. Cross-section microscopy of FGMs: (a) lamellar NiCrAlY–PSZ FGM processed by plasma spray technique (Sampath et al., 1995); (b) columnar ZrO_2–Y_2O_3 thermal barrier coating with graded porosity processed by electron beam physical vapor deposition (Kaysser and Ilschner, 1995).

relatively weak splat boundaries create an oriented material with higher stiffness and weak cleavage planes parallel to the boundary. Furthermore, graded materials processed by the *electron beam physical vapor*

deposition technique can have a columnar structure (Kaysser and Ilschner, 1995) (see Fig. 1(b)), which leads to a higher stiffness in the thickness direction and weak fracture planes perpendicular to the boundary. Thus, such materials would be orthotropic with preferential material directions that are perpendicular to each other. Gu and Asaro (1997) studied orthotropic FGMs considering a four-point bending specimen with varying Young's modulus and varying Poisson's ratio. Ozturk and Erdogan (1997, 1999) used integral equations to investigate mode I and mixed-mode crack problems in an infinite nonhomogeneous orthotropic medium with a crack aligned with one of the principal material directions considering constant Poisson's ratio. Kim and Paulino (2002c, 2003a) evaluated mixed-mode stress intensity factors (SIFs) for cracks arbitrarily oriented in orthotropic FGMs using the modified crack closure (MCC) method and the path-independent J_k^*-integral, respectively.

The interaction integral method is an accurate and robust scheme for evaluating mixed-mode SIFs. Yau et al. (1980) proposed the interaction integral method for evaluating SIFs in homogeneous isotropic materials. The method makes use of a conservation integral for two admissible states of an elastic solid: *actual* and *auxiliary*. Wang et al. (1980) extended the method to homogeneous orthotropic materials. Yau (1979) also used the method for bimaterial interface problems. Recently, the interaction integral method has been used for evaluating SIFs in isotropic FGMs (Dolbow and Gosz, 2002; Rao and Rahman, 2002; Kim and Paulino, 2003b,c). Dolbow and Gosz (2002) employed the extended finite element method; Rao and Rahman (2002) used the element-free Galerkin (EFG) method; Kim and Paulino (2003b) used the finite element method (FEM) to investigate FGMs with multiple cracks and material properties determined by means of either continuum functions (e.g. exponentially graded materials) or micromechanics models; and Kim and Paulino (2003c) have recently extended the method to evaluate the elastic T-stress. In the aforementioned papers (in this paragraph) the interaction integral method provided good accuracy for SIFs, however, it was investigated for isotropic FGMs only. *Thus the contribution of this work consists of developing the interaction integral method for orthotropic FGMs.*

This paper is organized as follows. Section 2 presents auxiliary fields appropriate for extracting SIFs from the interaction integral (M-integral [1]) method. Section 3 explains the M-integral formulation for orthotropic FGMs, its solution procedures and numerical aspects, and the relationships between M and SIFs. Section 4 presents the features of the finite element implementation. Section 5 presents various examples, which test different aspects of the proposed formulation. Finally, Section 6 presents some conclusions and potential extensions of this work.

2. Auxiliary fields

The presentation below follows Lekhnitskii's framework (Lekhnitskii, 1968). The generalized Hooke's law for stress–strain relationship is given by

$$\varepsilon_i = a_{ij}\sigma_j, \quad a_{ij} = a_{ji} \quad (i,j = 1,2,\ldots,6), \tag{1}$$

where the compliance coefficients, a_{ij}, are contracted notations of the compliance tensor S_{ijkl} and

$$\begin{aligned} &\varepsilon_1 = \varepsilon_{11}, \quad \varepsilon_2 = \varepsilon_{22}, \quad \varepsilon_3 = \varepsilon_{33}, \quad \varepsilon_4 = 2\varepsilon_{23}, \quad \varepsilon_5 = 2\varepsilon_{13}, \quad \varepsilon_6 = 2\varepsilon_{12}, \\ &\sigma_1 = \sigma_{11}, \quad \sigma_2 = \sigma_{22}, \quad \sigma_3 = \sigma_{33}, \quad \sigma_4 = \sigma_{23}, \quad \sigma_5 = \sigma_{13}, \quad \sigma_6 = \sigma_{12}. \end{aligned} \tag{2}$$

[1] Here, the so-called M-integral should not be confused with the M-integral (conservation integral) of Knowles and Sternberg (1972), Budiansky and Rice (1973), and Chang and Chien (2002). Also, see the book by Kanninen and Popelar (1985) for a review of conservation integrals in fracture mechanics.

For plane stress, the a_{ij} components of interest are

$$a_{ij} \quad (i,j = 1,2,6) \tag{3}$$

and for plane strain, the a_{ij} components are exchanged with b_{ij} as follows:

$$b_{ij} = a_{ij} - \frac{a_{i3}a_{j3}}{a_{33}} \quad (i,j = 1,2,6). \tag{4}$$

Two dimensional anisotropic elasticity problems can be formulated in terms of the analytic functions, $\phi_k(z_k)$, of the complex variable, $z_k = x_k + \mathrm{i}y_k$ $(k = 1,2)$, $\mathrm{i} = \sqrt{-1}$, where

$$x_k = x + \alpha_k y, \quad y_k = \beta_k y (k = 1,2). \tag{5}$$

The parameters α_k and β_k are the real and imaginary parts of $\mu_k = \alpha_k + \mathrm{i}\beta_k$, which can be determined from the following characteristic equation (Lekhnitskii, 1968)

$$a_{11}\mu^4 - 2a_{16}\mu^3 + (2a_{12} + a_{66})\mu^2 - 2a_{26}\mu + a_{22} = 0, \tag{6}$$

where the roots μ_k are always complex or purely imaginary in conjugate pairs as μ_1, $\overline{\mu_1}$; μ_2, $\overline{\mu_2}$.

2.1. Stress and displacement fields

Fig. 2 shows Cartesian and polar coordinate systems originating from a crack tip in an orthotropic FGM. For evaluating mixed-mode SIFs in FGMs, we select the auxiliary stress and displacement fields as the crack-tip asymptotic fields given by (see the paper by Sih et al. (1965) for the homogeneous case)

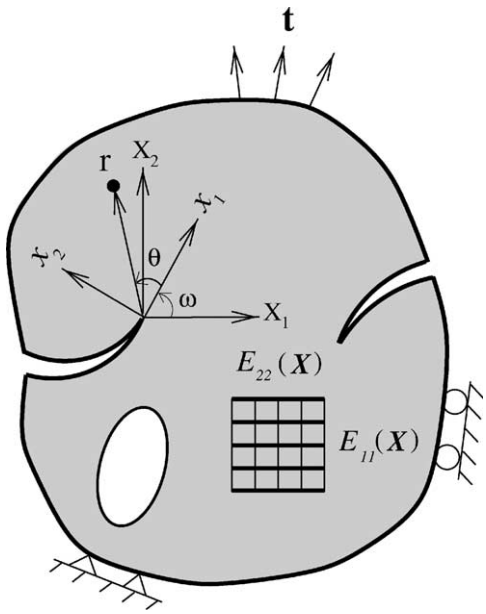

Fig. 2. Cartesian (x_1, x_2) and polar (r, θ) coordinates originating from the crack tip in an orthotropic nonhomogeneous material subjected to traction (**t**) and displacement boundary conditions.

$$
\begin{aligned}
\sigma_{11}^{\text{aux}} &= \frac{K_{\text{I}}^{\text{aux}}}{\sqrt{2\pi r}}\text{Re}\left[\frac{\mu_1^{\text{tip}}\mu_2^{\text{tip}}}{\mu_1^{\text{tip}}-\mu_2^{\text{tip}}}\left\{\frac{\mu_2^{\text{tip}}}{\sqrt{\cos\theta+\mu_2^{\text{tip}}\sin\theta}}-\frac{\mu_1^{\text{tip}}}{\sqrt{\cos\theta+\mu_1^{\text{tip}}\sin\theta}}\right\}\right] \\
&\quad+\frac{K_{\text{II}}^{\text{aux}}}{\sqrt{2\pi r}}\text{Re}\left[\frac{1}{\mu_1^{\text{tip}}-\mu_2^{\text{tip}}}\left\{\frac{(\mu_2^{\text{tip}})^2}{\sqrt{\cos\theta+\mu_2^{\text{tip}}\sin\theta}}-\frac{(\mu_1^{\text{tip}})^2}{\sqrt{\cos\theta+\mu_1^{\text{tip}}\sin\theta}}\right\}\right], \\
\sigma_{22}^{\text{aux}} &= \frac{K_{\text{I}}^{\text{aux}}}{\sqrt{2\pi r}}\text{Re}\left[\frac{1}{\mu_1^{\text{tip}}-\mu_2^{\text{tip}}}\left\{\frac{\mu_1^{\text{tip}}}{\sqrt{\cos\theta+\mu_2^{\text{tip}}\sin\theta}}-\frac{\mu_2^{\text{tip}}}{\sqrt{\cos\theta+\mu_1^{\text{tip}}\sin\theta}}\right\}\right] \\
&\quad+\frac{K_{\text{II}}^{\text{aux}}}{\sqrt{2\pi r}}\text{Re}\left[\frac{1}{\mu_1^{\text{tip}}-\mu_2^{\text{tip}}}\left\{\frac{1}{\sqrt{\cos\theta+\mu_2^{\text{tip}}\sin\theta}}-\frac{1}{\sqrt{\cos\theta+\mu_1^{\text{tip}}\sin\theta}}\right\}\right], \\
\sigma_{12}^{\text{aux}} &= \frac{K_{\text{I}}^{\text{aux}}}{\sqrt{2\pi r}}\text{Re}\left[\frac{\mu_1^{\text{tip}}\mu_2^{\text{tip}}}{\mu_1^{\text{tip}}-\mu_2^{\text{tip}}}\left\{\frac{1}{\sqrt{\cos\theta+\mu_1^{\text{tip}}\sin\theta}}-\frac{1}{\sqrt{\cos\theta+\mu_2^{\text{tip}}\sin\theta}}\right\}\right] \\
&\quad+\frac{K_{\text{II}}^{\text{aux}}}{\sqrt{2\pi r}}\text{Re}\left[\frac{1}{\mu_1^{\text{tip}}-\mu_2^{\text{tip}}}\left\{\frac{\mu_1^{\text{tip}}}{\sqrt{\cos\theta+\mu_1^{\text{tip}}\sin\theta}}-\frac{\mu_2^{\text{tip}}}{\sqrt{\cos\theta+\mu_2^{\text{tip}}\sin\theta}}\right\}\right]
\end{aligned}
\tag{7}
$$

and

$$
\begin{aligned}
u_1^{\text{aux}} &= K_{\text{I}}^{\text{aux}}\sqrt{\frac{2r}{\pi}}\text{Re}\left[\frac{1}{\mu_1^{\text{tip}}-\mu_2^{\text{tip}}}\left\{\mu_1^{\text{tip}}p_2\sqrt{\cos\theta+\mu_2^{\text{tip}}\sin\theta}-\mu_2^{\text{tip}}p_1\sqrt{\cos\theta+\mu_1^{\text{tip}}\sin\theta}\right\}\right] \\
&\quad+K_{\text{II}}^{\text{aux}}\sqrt{\frac{2r}{\pi}}\text{Re}\left[\frac{1}{\mu_1^{\text{tip}}-\mu_2^{\text{tip}}}\left\{p_2\sqrt{\cos\theta+\mu_2^{\text{tip}}\sin\theta}-p_1\sqrt{\cos\theta+\mu_1^{\text{tip}}\sin\theta}\right\}\right], \\
u_2^{\text{aux}} &= K_{\text{I}}^{\text{aux}}\sqrt{\frac{2r}{\pi}}\text{Re}\left[\frac{1}{\mu_1^{\text{tip}}-\mu_2^{\text{tip}}}\left\{\mu_1^{\text{tip}}q_2\sqrt{\cos\theta+\mu_2^{\text{tip}}\sin\theta}-\mu_2^{\text{tip}}q_1\sqrt{\cos\theta+\mu_1^{\text{tip}}\sin\theta}\right\}\right] \\
&\quad+K_{\text{II}}^{\text{aux}}\sqrt{\frac{2r}{\pi}}\text{Re}\left[\frac{1}{\mu_1^{\text{tip}}-\mu_2^{\text{tip}}}\left\{q_2\sqrt{\cos\theta+\mu_2^{\text{tip}}\sin\theta}-q_1\sqrt{\cos\theta+\mu_1^{\text{tip}}\sin\theta}\right\}\right],
\end{aligned}
\tag{8}
$$

respectively, where Re denotes the real part of the complex function, μ_1^{tip} and μ_2^{tip} denote crack-tip material parameters evaluated by using Eq. (6), which are taken for $\beta_k > 0$ $(k = 1, 2)$, and p_k and q_k are given by

$$
\begin{aligned}
p_k &= a_{11}^{\text{tip}}(\mu_k^{\text{tip}})^2 + a_{12}^{\text{tip}} - a_{16}^{\text{tip}}\mu_k^{\text{tip}}, \\
q_k &= a_{12}^{\text{tip}}\mu_k^{\text{tip}} + \frac{a_{22}^{\text{tip}}}{\mu_k^{\text{tip}}} - a_{26}^{\text{tip}},
\end{aligned}
\tag{9}
$$

respectively. Notice that in the above expressions, the material parameters are sampled at the crack tip. Moreover, the auxiliary stress fields in Eq. (7) are in equilibrium, i.e. $\sigma_{ij,j}^{\text{aux}} = 0$ (no body forces or inertia effects).

2.2. Strain field—incompatibility formulation

The auxiliary strain field is chosen as

$$\varepsilon_{ij}^{\text{aux}} = S_{ijkl}(\boldsymbol{x})\sigma_{kl}^{\text{aux}}, \tag{10}$$

which differs from

$$\varepsilon_{ij}^{\text{aux}} = (S_{ijkl})_{\text{tip}}\sigma_{kl}^{\text{aux}}, \tag{11}$$

where $S_{ijkl}(\boldsymbol{x})$ is the compliance tensor of the actual FGM and $(S_{ijkl})_{\text{tip}}$ is the compliance tensor at the crack tip and, in general, $S_{ijkl}(\boldsymbol{x}) \neq (S_{ijkl})_{\text{tip}}$ for $\boldsymbol{x} \neq \boldsymbol{0}$ as shown in Fig. 3. Thus, the auxiliary strain field in Eq. (10) is incompatible with the symmetric part of the auxiliary displacement gradient of Eq. (8), i.e.

$$\varepsilon_{ij}^{\text{aux}} \neq (u_{i,j}^{\text{aux}} + u_{j,i}^{\text{aux}})/2. \tag{12}$$

Although this incompatibility of the strain field vanishes as the contour shrinks to the crack tip, it gives finite contributions for finite domains. Thus, it must be considered in the formulation, and cannot be neglected.

2.3. Some remarks on alternative formulations

An alternative for the auxiliary fields is to use the auxiliary stress and displacement fields as given by Eqs. (7) and (8), respectively, and to evaluate the auxiliary strain fields by using the symmetric gradient of the auxiliary displacement fields of Eq. (8). For this choice of the stress and strain fields, the stress–strain relationship is given by

$$\sigma_{ij}^{\text{aux}} = (C_{ijkl})_{\text{tip}}\varepsilon_{kl}^{\text{aux}}, \tag{13}$$

where $(C_{ijkl})_{\text{tip}}$ is a constant constitutive tensor evaluated at the crack tip. Thus the constitutive relation is only satisfied at the crack tip location and, in general, it is not satisfied elsewhere, i.e. $C_{ijkl}(\boldsymbol{x}) \neq (C_{ijkl})_{\text{tip}}$. Moreover, the auxiliary stress fields are in equilibrium and the auxiliary strain fields are compatible with the

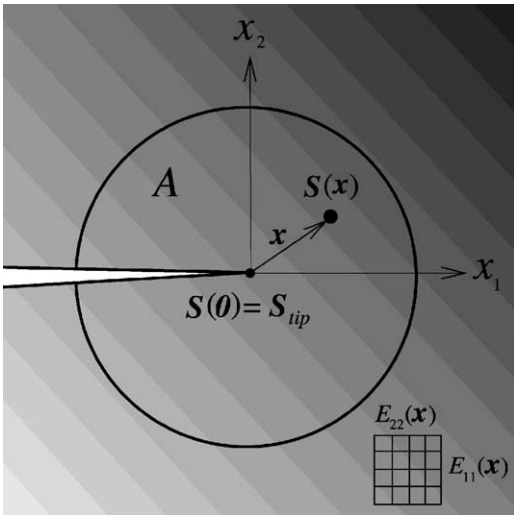

Fig. 3. Illustration of the "incompatibility formulation" accounting for material nonhomogeneity. Notice that, in general, $\boldsymbol{S}(\boldsymbol{x}) \neq \boldsymbol{S}_{\text{tip}}$ for $\boldsymbol{x} \neq \boldsymbol{0}$. The area A denotes a representative region around the crack tip.

auxiliary displacement fields. Dolbow and Gosz (2002) discussed this choice of auxiliary fields. Rao and Rahman (2002) used these auxiliary fields (referred to as Method I in their paper) and implemented them using the EFG numerical method.

Another alternative for the auxiliary fields is to choose the auxiliary strain fields by using the symmetric gradient of the auxiliary displacement fields of Eq. (8), and to evaluate the auxiliary stress fields as follows:

$$\sigma_{ij}^{\text{aux}} = C_{ijkl}(\boldsymbol{x})\varepsilon_{kl}^{\text{aux}}. \tag{14}$$

Notice that the auxiliary stress field is not in equilibrium, i.e. $\sigma_{ij,j}^{\text{aux}} \neq 0$ (no body forces). In this case, the auxiliary strain field is compatible with the auxiliary displacement field $\varepsilon_{ij}^{\text{aux}} = (u_{i,j}^{\text{aux}} + u_{j,i}^{\text{aux}})/2$. This formulation is the dual counterpart to the incompatibility formulation, and the nonequilibrium formulation is given by Kim and Paulino (submitted for publication). This choice of the auxiliary fields has also been discussed by Dolbow and Gosz (2002).

3. The interaction integral: *M*-integral

The interaction integral (M-integral) is derived from the path-independent J-integral (Rice, 1968) for two admissible states of a cracked elastic orthotropic FGM. For the sake of numerical efficiency using a domain-based method such as the FEM, the contour integral is transformed into an equivalent domain integral (EDI) (Raju and Shivakumar, 1990). The theoretical formulation, the solution procedure, numerical aspects, and the extraction of mixed-mode SIFs are provided below.

3.1. M-integral: incompatibility formulation

The standard J-integral (Rice, 1968) is given by

$$J = \lim_{\Gamma_s \to 0} \int_{\Gamma_s} (\mathscr{W}\delta_{1j} - \sigma_{ij}u_{i,1})n_j \,\mathrm{d}\Gamma, \tag{15}$$

where $\mathscr{W}$ is the strain energy density expressed by

$$\mathscr{W} = \frac{1}{2}\sigma_{ij}\varepsilon_{ij} = \frac{1}{2}C_{ijkl}\varepsilon_{kl}\varepsilon_{ij}, \tag{16}$$

and n_j is the outward normal vector to the contour Γ_s, as shown in Fig. 4. Let us define the following contour integral:

$$\mathscr{H} = \oint_{\Gamma} (\mathscr{W}\delta_{1j} - \sigma_{ij}u_{i,1})m_j q \,\mathrm{d}\Gamma, \tag{17}$$

where $\Gamma = \Gamma_o + \Gamma^+ - \Gamma_s + \Gamma^-$, m_j is a unit outward normal vector to the corresponding contour (i.e. $m_j = n_j$ on Γ_o and $m_j = -n_j$ on Γ_s), and q is a weight function defined as a smoothly varying function from $q = 1$ on Γ_s to $q = 0$ on Γ_o (see Fig. 5). Taking the limit $\Gamma_s \to 0$, one obtains

$$\begin{aligned}
\lim_{\Gamma_s \to 0} \mathscr{H} &= \lim_{\Gamma_s \to 0} \int_{\Gamma_o + \Gamma^+ + \Gamma^- - \Gamma_s} (\mathscr{W}\delta_{1j} - \sigma_{ij}u_{i,1})m_j q \,\mathrm{d}\Gamma \\
&= \lim_{\Gamma_s \to 0} \left[\int_{\Gamma_o + \Gamma^+ + \Gamma^-} (\mathscr{W}\delta_{1j} - \sigma_{ij}u_{i,1})m_j q \,\mathrm{d}\Gamma + \int_{-\Gamma_s} (\mathscr{W}\delta_{1j} - \sigma_{ij}u_{i,1})m_j q \,\mathrm{d}\Gamma \right] \\
&= \lim_{\Gamma_s \to 0} \left[\int_{\Gamma_o + \Gamma^+ + \Gamma^-} (\mathscr{W}\delta_{1j} - \sigma_{ij}u_{i,1})m_j q \,\mathrm{d}\Gamma - \int_{\Gamma_s} (\mathscr{W}\delta_{1j} - \sigma_{ij}u_{i,1})n_j q \,\mathrm{d}\Gamma \right].
\end{aligned} \tag{18}$$

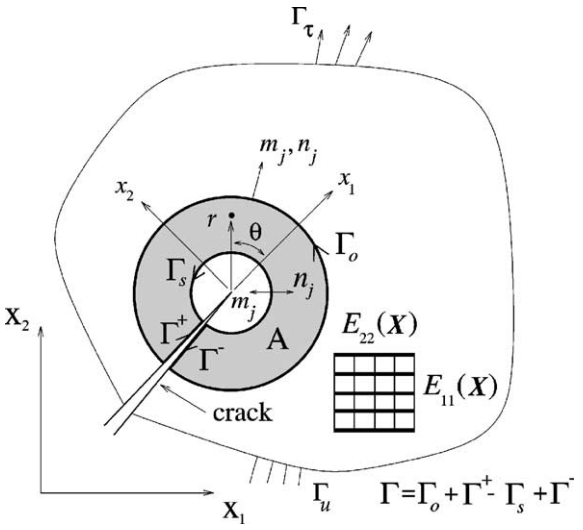

Fig. 4. Conversion of the contour integral into an equivalent domain integral (EDI) where $\Gamma = \Gamma_o + \Gamma^+ - \Gamma_s + \Gamma^-$, $m_j = n_j$ on Γ_o and $m_j = -n_j$ on Γ_s.

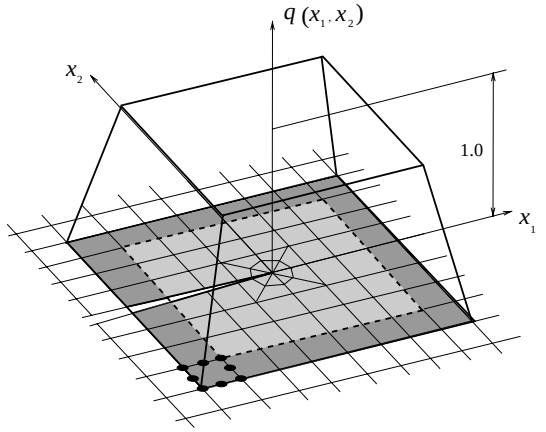

Fig. 5. Plateau weight function (q-function).

Because $q = 0$ on Γ_o and the crack faces are assumed to be traction-free, Eq. (18) becomes

$$J = -\lim_{\Gamma_s \to 0} \mathscr{H} = -\lim_{\Gamma_s \to 0} \oint_\Gamma (\mathscr{W}\delta_{1j} - \sigma_{ij}u_{i,1}) m_j q \, \mathrm{d}\Gamma. \tag{19}$$

Applying the divergence theorem to Eq. (19), one obtains the following EDI

$$J = \int_A (\sigma_{ij}u_{i,1} - \mathscr{W}\delta_{1j}) q_{,j} \, \mathrm{d}A + \int_A (\sigma_{ij}u_{i,1} - \mathscr{W}\delta_{1j})_{,j} q \, \mathrm{d}A. \tag{20}$$

Using the derivative of strain energy density given by

$$\mathscr{W}_{,1} = \frac{\partial \mathscr{W}}{\partial x_1} = \sigma_{ij}\varepsilon_{ij,1} + \frac{1}{2} C_{ijkl,1}\varepsilon_{kl}\varepsilon_{ij}, \tag{21}$$

one obtains

$$J = \int_A (\sigma_{ij} u_{i,1} - \mathscr{W}\delta_{1j}) q_{,j}\,\mathrm{d}A + \int_A \left\{ \underline{\sigma_{ij}(u_{i,1j} - \varepsilon_{ij,1})} - \frac{1}{2} C_{ijkl,1}\varepsilon_{kl}\varepsilon_{ij} \right\} q\,\mathrm{d}A. \tag{22}$$

The underlined terms in Eq. (22) must vanish for the actual fields, but we retain them to extract the incompatible term for the auxiliary fields. For two admissible fields, which are taken as the actual $(\boldsymbol{u}, \boldsymbol{\varepsilon}, \boldsymbol{\sigma})$ and auxiliary $(\boldsymbol{u}^{\mathrm{aux}}, \boldsymbol{\varepsilon}^{\mathrm{aux}}, \boldsymbol{\sigma}^{\mathrm{aux}})$ fields, the superimposed J-integral, J^{s}, is given by

$$J^{\mathrm{s}} = J + J^{\mathrm{aux}} + M, \tag{23}$$

where J is given by Eq. (22), J^{aux} is given by

$$J^{\mathrm{aux}} = \int_A (\sigma_{ij}^{\mathrm{aux}} u_{i,1}^{\mathrm{aux}} - \mathscr{W}^{\mathrm{aux}}\delta_{1j}) q_{,j}\,\mathrm{d}A + \int_A \left\{ \sigma_{ij}^{\mathrm{aux}}(u_{i,1j}^{\mathrm{aux}} - \varepsilon_{ij,1}^{\mathrm{aux}}) - \frac{1}{2} C_{ijkl,1}\varepsilon_{kl}^{\mathrm{aux}}\varepsilon_{ij}^{\mathrm{aux}} \right\} q\,\mathrm{d}A, \tag{24}$$

and M is the interaction integral (i.e. with the integrand given by terms involving products of the actual and auxiliary fields) given by [2]

$$\begin{aligned} M = & \int_A \left\{ (\sigma_{ij} u_{i,1}^{\mathrm{aux}} + \sigma_{ij}^{\mathrm{aux}} u_{i,1}) - \frac{1}{2}(\sigma_{ik}\varepsilon_{ik}^{\mathrm{aux}} + \sigma_{ik}^{\mathrm{aux}}\varepsilon_{ik})\delta_{1j} \right\} q_{,j}\,\mathrm{d}A \\ & + \int_A \left\{ \sigma_{ij}(u_{i,1j}^{\mathrm{aux}} - \varepsilon_{ij,1}^{\mathrm{aux}}) + \sigma_{ij}^{\mathrm{aux}}(u_{i,1j} - \varepsilon_{ij,1}) - \frac{1}{2} C_{ijkl,1}(\varepsilon_{ij}\varepsilon_{kl}^{\mathrm{aux}} + \varepsilon_{ij}^{\mathrm{aux}}\varepsilon_{kl}) \right\} q\,\mathrm{d}A. \end{aligned} \tag{25}$$

After algebraic manipulations involving the following equalities

$$\sigma_{ij}^{\mathrm{aux}} u_{i,1j} = \sigma_{ij}^{\mathrm{aux}}\varepsilon_{ij,1}, \quad \sigma_{ij}\varepsilon_{ij}^{\mathrm{aux}} = \sigma_{ij}^{\mathrm{aux}}\varepsilon_{ij}, \quad C_{ijkl,1}\varepsilon_{ij}^{\mathrm{aux}}\varepsilon_{kl} = C_{ijkl,1}\varepsilon_{ij}\varepsilon_{kl}^{\mathrm{aux}}, \tag{26}$$

one obtains

$$\begin{aligned} M &= (M_1)_{\mathrm{local}} \\ &= \int_A \left\{ (\sigma_{ij} u_{i,1}^{\mathrm{aux}} + \sigma_{ij}^{\mathrm{aux}} u_{i,1}) - \frac{1}{2}(\sigma_{ik}\varepsilon_{ik}^{\mathrm{aux}} + \sigma_{ik}^{\mathrm{aux}}\varepsilon_{ik})\delta_{1j} \right\} q_{,j}\,\mathrm{d}A + \int_A \{ \underline{\sigma_{ij}(u_{i,1j}^{\mathrm{aux}} - \varepsilon_{ij,1}^{\mathrm{aux}})} - C_{ijkl,1}\varepsilon_{ij}\varepsilon_{kl}^{\mathrm{aux}} \} q\,\mathrm{d}A. \end{aligned} \tag{27}$$

Notice that the incompatible term, underlined in Eq. (27), arises naturally in the M-integral formulation for FGMs, but vanishes for homogeneous materials.

3.2. M-integral: numerical aspects

Due to the nature of the FEM, the M-integral is evaluated first in the global coordinates (M_{global}) and then transformed to the local coordinates (M_{local}). The global interaction integral $(M_m)_{\mathrm{global}}$ is obtained as $(m = 1, 2)$

$$\begin{aligned} (M_m)_{\mathrm{global}} = & \int_A \left\{ (\sigma_{ij} u_{i,m}^{\mathrm{aux}} + \sigma_{ij}^{\mathrm{aux}} u_{i,m}) - \frac{1}{2}(\sigma_{ik}\varepsilon_{ik}^{\mathrm{aux}} + \sigma_{ik}^{\mathrm{aux}}\varepsilon_{ik})\delta_{mj} \right\} \frac{\partial q}{\partial X_j}\,\mathrm{d}A \\ & + \int_A \left\{ \underline{\sigma_{ij}(u_{i,mj}^{\mathrm{aux}} - \varepsilon_{ij,m}^{\mathrm{aux}})} - C_{ijkl,m}\varepsilon_{ij}\varepsilon_{kl}^{\mathrm{aux}} \right\} q\,\mathrm{d}A, \end{aligned} \tag{28}$$

[2] Notice that the M-integral here is different from the conservation integral (also denoted by M) of Knowles and Sternberg (1972), Budiansky and Rice (1973), Chang and Chien (2002), and Kanninen and Popelar (1985). In these references $M = \int_\Gamma (\mathscr{W}\delta_{ij} - \sigma_{kj}u_{k,i}) n_j x_i\,\mathrm{d}s$ (for two dimensional problems).

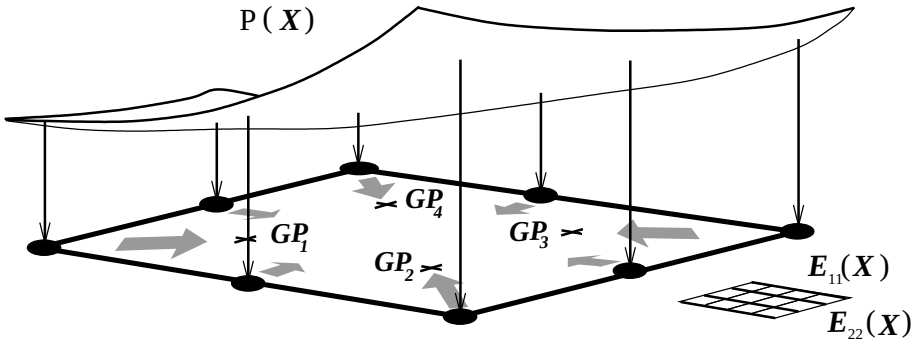

Fig. 6. Generalized isoparametric formulation (GIF) (Kim and Paulino, 2002a,b) using graded finite elements. The above figure illustrates a graded Q8 element and $P(\boldsymbol{X})$ denotes a generic material property, e.g. stiffness tensor components (C_{ijkl}) or compliance tensor components (S_{ijkl}). The material properties at the Gauss points (P_{GP}) are interpolated from nodal material properties (P_i) by $P_{\mathrm{GP}} = \sum N_i P_i$ where $\boldsymbol{N}$ are element shape functions.

where (X_1, X_2) are global coordinates as illustrated by Fig. 4. The local M-integral (M_{local}) is calculated by transformation as

$$M_{\mathrm{local}} = (M_1)_{\mathrm{global}} \cos\theta + (M_2)_{\mathrm{global}} \sin\theta. \tag{29}$$

In Eq. (28), special consideration should be taken for the derivatives of the constitutive tensor $C_{ijkl,m}$ and the derivatives of the auxiliary strain field $\varepsilon^{\mathrm{aux}}_{ij,m}$, which is given by

$$\varepsilon^{\mathrm{aux}}_{ij,m} = S_{ijkl,m}\sigma^{\mathrm{aux}}_{kl} + S_{ijkl}\sigma^{\mathrm{aux}}_{kl,m}. \tag{30}$$

A simple and accurate approach to evaluate $C_{ijkl,m}$ (see Eq. (28)) and $S_{ijkl,m}$ (see Eq. (30)) is to use shape function derivatives. The derivatives of the material quantity $P \equiv P(\boldsymbol{X})$ (e.g. C_{ijkl} and S_{ijkl}) are obtained as (cf. Fig. 6):

$$\frac{\partial P}{\partial X_m} = \sum_{i=1}^{n} \frac{\partial N_i}{\partial X_m} P_i, \quad (m = 1, 2), \tag{31}$$

where n is the number of element nodes and $N_i = N_i(\xi, \eta)$ are the shape functions which can be found in many references, e.g. Cook et al. (2002). The derivatives $\partial N_i/\partial X_m$ are obtained as

$$\begin{Bmatrix} \partial N_i/\partial X_1 \\ \partial N_i/\partial X_2 \end{Bmatrix} = \boldsymbol{J}^{-1} \begin{Bmatrix} \partial N_i/\partial \xi \\ \partial N_i/\partial \eta \end{Bmatrix}, \tag{32}$$

where $\boldsymbol{J}^{-1}$ is the inverse of the standard Jacobian matrix given by

$$\boldsymbol{J} = \begin{bmatrix} \partial X_1/\partial \xi & \partial X_2/\partial \xi \\ \partial X_1/\partial \eta & \partial X_2/\partial \eta \end{bmatrix}. \tag{33}$$

Furthermore, the details on how to determine the auxiliary strain fields with respect to the global coordinates are explained in Appendix A.

3.3. M-integral: extraction of stress intensity factors

For mixed-mode crack problems, the energy release rates $\mathscr{G}_{\mathrm{I}}$ and $\mathscr{G}_{\mathrm{II}}$ are related to mixed-mode SIFs as follows:

$$\mathcal{G}_{\mathrm{I}} = -\frac{K_{\mathrm{I}}}{2} a_{22}^{\mathrm{tip}} \operatorname{Im}\left[\frac{K_{\mathrm{I}}(\mu_1^{\mathrm{tip}} + \mu_2^{\mathrm{tip}}) + K_{\mathrm{II}}}{\mu_1^{\mathrm{tip}} \mu_2^{\mathrm{tip}}}\right],$$
$$\mathcal{G}_{\mathrm{II}} = \frac{K_{\mathrm{II}}}{2} a_{11}^{\mathrm{tip}} \operatorname{Im}[K_{\mathrm{II}}(\mu_1^{\mathrm{tip}} + \mu_2^{\mathrm{tip}}) + K_{\mathrm{I}}(\mu_1^{\mathrm{tip}} \mu_2^{\mathrm{tip}})], \tag{34}$$

where Im denotes the imaginary part of the complex function. Thus

$$J_{\mathrm{local}} = \mathcal{G} = \mathcal{G}_{\mathrm{I}} + \mathcal{G}_{\mathrm{II}} = c_{11} K_{\mathrm{I}}^2 + c_{12} K_{\mathrm{I}} K_{\mathrm{II}} + c_{22} K_{\mathrm{II}}^2, \tag{35}$$

where

$$c_{11} = -\frac{a_{22}^{\mathrm{tip}}}{2} \operatorname{Im}\left(\frac{\mu_1^{\mathrm{tip}} + \mu_2^{\mathrm{tip}}}{\mu_1^{\mathrm{tip}} \mu_2^{\mathrm{tip}}}\right),$$
$$c_{12} = -\frac{a_{22}^{\mathrm{tip}}}{2} \operatorname{Im}\left(\frac{1}{\mu_1^{\mathrm{tip}} \mu_2^{\mathrm{tip}}}\right) + \frac{a_{11}^{\mathrm{tip}}}{2} \operatorname{Im}\left(\mu_1^{\mathrm{tip}} \mu_2^{\mathrm{tip}}\right), \tag{36}$$
$$c_{22} = \frac{a_{11}^{\mathrm{tip}}}{2} \operatorname{Im}(\mu_1^{\mathrm{tip}} + \mu_2^{\mathrm{tip}}).$$

For two admissible fields, which are the actual $(\boldsymbol{u}, \boldsymbol{\varepsilon}, \boldsymbol{\sigma})$ and auxiliary $(\boldsymbol{u}^{\mathrm{aux}}, \boldsymbol{\varepsilon}^{\mathrm{aux}}, \boldsymbol{\sigma}^{\mathrm{aux}})$ fields, one obtains (Wang et al., 1980)

$$J_{\mathrm{local}}^{\mathrm{s}} = c_{11}(K_{\mathrm{I}} + K_{\mathrm{I}}^{\mathrm{aux}})^2 + c_{12}(K_{\mathrm{I}} + K_{\mathrm{I}}^{\mathrm{aux}})(K_{\mathrm{II}} + K_{\mathrm{II}}^{\mathrm{aux}}) + c_{22}(K_{\mathrm{II}} + K_{\mathrm{II}}^{\mathrm{aux}})^2 = J_{\mathrm{local}} + J_{\mathrm{local}}^{\mathrm{aux}} + M_{\mathrm{local}}, \tag{37}$$

where J_{local} is given by Eq. (35), $J_{\mathrm{local}}^{\mathrm{aux}}$ is given by

$$J_{\mathrm{local}}^{\mathrm{aux}} = c_{11}(K_{\mathrm{I}}^{\mathrm{aux}})^2 + c_{12} K_{\mathrm{I}}^{\mathrm{aux}} K_{\mathrm{II}}^{\mathrm{aux}} + c_{22}(K_{\mathrm{II}}^{\mathrm{aux}})^2 \tag{38}$$

and M_{local} is given by

$$M_{\mathrm{local}} = 2c_{11} K_{\mathrm{I}} K_{\mathrm{I}}^{\mathrm{aux}} + c_{12}(K_{\mathrm{I}} K_{\mathrm{II}}^{\mathrm{aux}} + K_{\mathrm{I}}^{\mathrm{aux}} K_{\mathrm{II}}) + 2c_{22} K_{\mathrm{II}} K_{\mathrm{II}}^{\mathrm{aux}}. \tag{39}$$

The mode I and mode II SIFs are evaluated by solving the following linear algebraic equations:

$$M_{\mathrm{local}}^{(1)} = 2c_{11} K_{\mathrm{I}} + c_{12} K_{\mathrm{II}} \quad (K_{\mathrm{I}}^{\mathrm{aux}} = 1.0, K_{\mathrm{II}}^{\mathrm{aux}} = 0.0), \tag{40}$$

$$M_{\mathrm{local}}^{(2)} = c_{12} K_{\mathrm{I}} + 2c_{22} K_{\mathrm{II}} \quad (K_{\mathrm{I}}^{\mathrm{aux}} = 0.0, K_{\mathrm{II}}^{\mathrm{aux}} = 1.0). \tag{41}$$

The relationships of Eqs. (40) and (41) are the same as those for homogeneous orthotropic materials (Wang et al., 1980) except that, for FGMs, the material properties are evaluated at the crack-tip location. Notice that there is no need for Newton's iteration, which is needed with other approaches such as the path-independent J_k-integral (Kim and Paulino, 2003a) and the MCC (Kim and Paulino, 2002c). Here the SIFs for mode I and mode II are decoupled (cf. Eqs. (40) and (41)).

4. FEM implementation

The FEM code I-FRANC2D (Illinois-FRANC2D) has been used for implementation of the present interaction integral formulation, and for obtaining all the numerical results presented in this paper. I-FRANC2D is based on the FRANC2D (FRacture ANalysis Code 2D) (Wawrzynek, 1987; Wawrzynek and Ingraffea, 1991), which was originally developed at Cornell University. The extended capabilities of I-FRANC2D include graded elements (see Fig. 6) to discretize nonhomogeneous materials, and fracture parameters such as mixed-mode SIFs and T-stress. The I-FRANC2D material library contains continuum

functions (e.g. exponential, linear, hyperbolic-tangent, and radial functions) and micromechanics models (e.g. self-consistent, Mori-Tanaka, and three-phase model).

The graded elements are based on the "generalized isoparametric formulation" or GIF (Kim and Paulino, 2002a,b) and, in general, they show superior performance to conventional homogeneous elements (element-wise constant material property) (Kim and Paulino, 2002b). Using graded elements, the I-FRANC2D FEM code can evaluate SIFs for both isotropic and orthotropic FGMs by using the interaction integral. The code also has other numerical schemes especially tailored for FGMs (Kim and Paulino, 2002a) such as the path-independent J_k^*-integral, the MCC, and the displacement correlation technique (DCT) for both isotropic and orthotropic FGMs (Kim and Paulino, 2002a,c, 2003a). Based on numerical investigations, Kim and Paulino (2003b,c) observed that the interaction integral scheme provides good accuracy in comparison with the above-mentioned schemes for isotropic FGMs. This paper shows that this is also the case for orthotropic FGMs.

5. Examples

The performance of the interaction integral for evaluating SIFs in orthotropic FGMs is examined by means of numerical examples. In order to assess the various features of the method, the following examples are presented:

(1) Plate with a crack parallel to the material gradation.
(2) Plate with a crack perpendicular to the material gradation.
(3) Four-point bending specimen.
(4) Disk with an inclined center crack.
(5) Plate with a curved crack.
(6) Strip with an edge crack.

Isoparametric graded elements are used to discretize the geometry of all the above examples. Singular quarter-point six-node triangles (T6qp) are used for crack-tip elements, eight-node serendipity elements (Q8) are used for a circular region around crack-tip elements and over most of the mesh, and regular six-node triangles (T6) are used in the transition zone between regions of Q8 elements.

All the examples report SIFs or energy release rates obtained by means of the interaction integral in conjunction with the FEM. The first and second examples are presented as a means to validate the implementation against the semi-analytical solutions by Ozturk and Erdogan (1997, 1999). The third example is also presented as a validation of the implementation against the solutions reported by Gu and Asaro (1997). The fourth example investigates an inclined center crack in a circular disk with material gradation both in radial and Cartesian directions. The fifth example investigates a semi-circular crack. Finally, the last example investigates an edge crack in hyperbolic tangent materials considering various translations of material properties.

The first two examples employ the following averaged material parameters: the effective Young's modulus E, the effective Poisson's ratio v, the stiffness ratio δ^4 and the shear parameter κ_0. They replace the independent engineering constants E_{ii}, G_{ij} and v_{ij} $((v_{ij}/E_{ii}) = (v_{ji}/E_{jj}))$ $(i,j = 1,2)$, i.e. (Krenk, 1979)

$$E = \sqrt{E_{11}E_{22}}, \quad v = \sqrt{v_{12}v_{21}}, \quad \delta^4 = \frac{E_{11}}{E_{22}} = \frac{v_{12}}{v_{21}}, \quad \kappa_0 = \frac{E}{2G_{12}} - v, \tag{42}$$

for plane stress. The bounds on Poisson's ratios v_{12} and v_{21} for plane orthotropy are given by (Christensen, 1979):

$$|\nu_{12}| < (E_{11}/E_{22})^{1/2}, \quad |\nu_{21}| < (E_{22}/E_{11})^{1/2}, \tag{43}$$

respectively. Therefore the bound on the effective Poisson's ratio [3] is $\nu < 1.0$. The first two examples also consider proportional material nonhomogeneity, i.e.

$$\beta = \frac{1}{2H}\log\left[\frac{E_{11}(H)}{E_{11}(-H)}\right] = \frac{1}{2H}\log\left[\frac{E_{22}(H)}{E_{22}(-H)}\right] = \frac{1}{2H}\log\left[\frac{G_{12}(H)}{G_{12}(-H)}\right], \tag{44}$$

where H is the length of material gradation considered, e.g. $H = W$ for the first example and $H = L$ for the second example. The nonhomogeneity parameter β has units $[\text{length}]^{-1}$.

5.1. Plate with a crack parallel to material gradation

Fig. 7(a)–(d) show a center crack of length $2a$ located in a finite two-dimensional plate under fixed grip loading or constant traction, the complete finite element mesh, a mesh detail with 16 sectors (S16) and four rings (R4) around crack tips, and a zoom of the right crack tip region, respectively. For fixed-grip loading, the applied load results in uniform strain $\varepsilon_{22}(X_1, X_2) = \varepsilon_0$ for a corresponding uncracked plate; and for constant traction, the applied load $\sigma_{22}(X_1, \pm L) = \pm 1.0$ along the top and bottom edges. The displacement boundary conditions are prescribed such that $u_1 = u_2 = 0$ for the center node on the left edge, and $u_2 = 0$ for the center node on the right edge.

The variations of E_{11}, E_{22}, and G_{12} are assumed to be an exponential function of X_1 and *proportional* to one another, while the Poisson's ratio ν_{12} is constant. The mesh has 1666 Q8, 303 T6, and 32 T6qp crack-tip singular elements with a total of 2001 elements and 5851 nodes (see Fig. 7(b)). The following data were used for the FEM analysis:

$$\begin{aligned}
&a/W = 0.1, \quad L/W = 1.0, \quad \varepsilon_0 = 1.0, \quad \beta a = 0.5,\\
&E_{11}(X_1) = E_{11}^0 \mathrm{e}^{\beta X_1}, \quad E_{22}(X_1) = E_{22}^0 \mathrm{e}^{\beta X_1}, \quad G_{12}(X_1) = G_{12}^0 \mathrm{e}^{\beta X_1},\\
&\kappa_0 = 0.5, \ \nu = (0.1, 0.2, 0.3, 0.4, 0.5, 0.7, 0.9),\\
&\text{plane stress}, \ \ 2 \times 2 \text{ Gauss quadrature.}
\end{aligned} \tag{45}$$

Table 1 shows the effect of material nonhomogeneity on normalized mode I SIF for the nonhomogeneous orthotropic plate of Fig. 7 under fixed grip loading considering $\nu = 0.3$ and $\kappa_0 = 0.5$. The FEM results obtained by the interaction integral agree very well with those obtained by the MCC (Kim and Paulino, 2002c). As the dimensionless nonhomogeneity parameter βa increases, the mode I SIF at the right crack tip increases, but the mode I SIF at the left crack tip decreases. This is expected due to the nature of the exponential material gradation with the origin of the Cartesian coordinate system at the center of the plate. Table 2 shows the effect of the Poisson's ratio ν on mode I SIF for the nonhomogeneous orthotropic plate of Fig. 7 under fixed grip loading considering $\beta a = 0.5$ and $\kappa_0 = 0.5$. The FEM results obtained by means of the M-integral agree with the SIFs obtained by Ozturk and Erdogan (1997) to within 1%. The effective Poisson's ratio $\nu = \sqrt{\nu_{12}\nu_{21}}$ has a negligible effect on the SIFs for a mode I crack problem. With respect to the M-integral, notice that the results of Table 1 considering $\beta a = 0.5$ coincide with those of Table 2 for $\nu = 0.3$. These results are presented in bold at these Tables. In order to assess the accuracy of the present interaction integral method (M-integral), Table 3 shows normalized SIFs computed by other methods, such as J_k^*-integral, the MCC, and the DCT. By comparing Tables 2 and 3, and adopting Ozturk and Erdogan's (1997) semi-analytical solution as reference, the interaction integral provides the best accuracy with respect to the aforementioned schemes.

[3] Notice that the effective Poisson's ratio ν (see Eq. (42)) can be bigger than 0.5 for orthotropic materials.

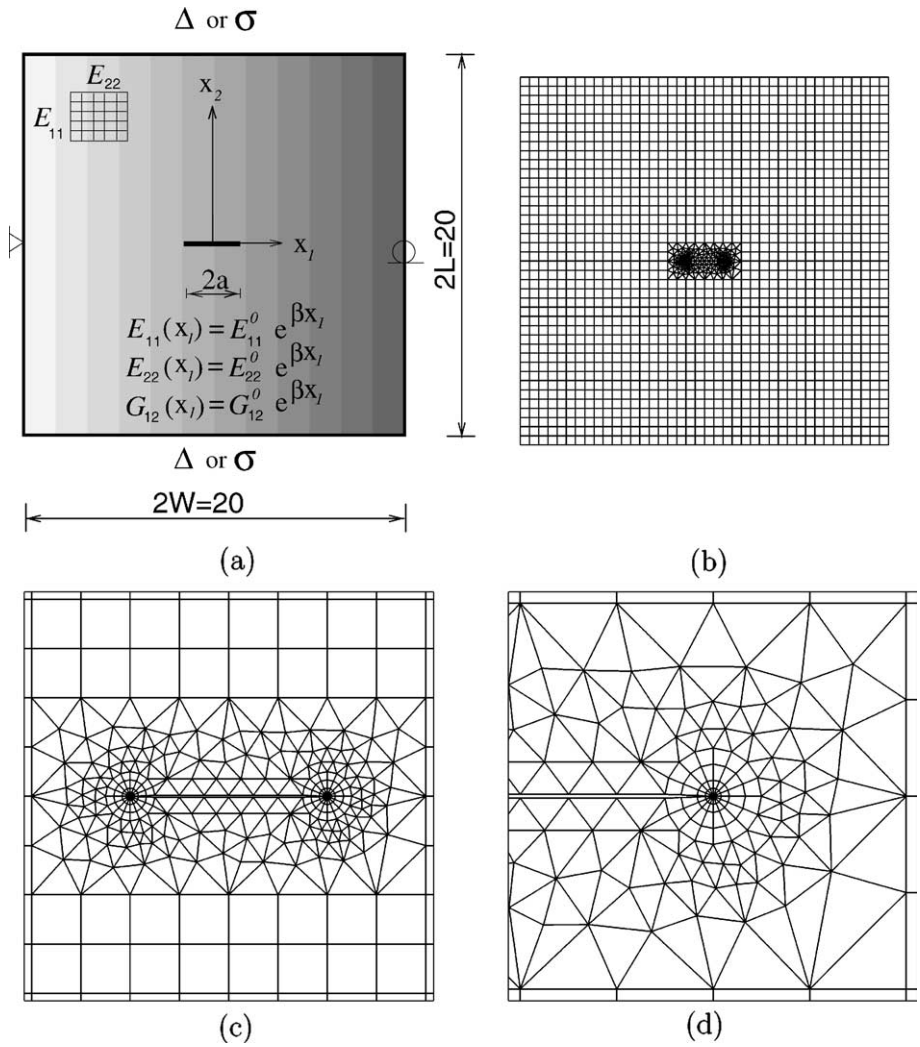

Fig. 7. Example 1: plate with a center crack parallel to the material gradation: (a) geometry and BCs considering either fixed-grip loading (Δ) or far-field traction (σ) on the (far-field) horizontal edges; (b) complete finite element mesh; (c) mesh detail using 16 sectors (S16) and 4 rings (R4) around crack tips; (d) zoom of the right crack tip.

Table 1
Example 1: the effect of material nonhomogeneity on normalized mode I SIF in a nonhomogeneous orthotropic plate under fixed grip loading ($v = 0.3$, $\kappa_0 = 0.5$, $K_0 = \varepsilon_0 \overline{E}^0 \sqrt{\pi a}$; $\overline{E}^0 = E^0/\delta^2$; $E^0 = \sqrt{E_{11}^0 E_{22}^0}$) (see Fig. 7)

βa	M-integral (present)		MCC	
	$K_I(+a)/K_0$	$K_I(-a)/K_0$	$K_I(+a)/K_0$	$K_I(-a)/K_0$
0.00	0.9969	0.9969	0.9986	0.9986
0.10	1.0750	0.9247	1.0791	0.9251
0.25	1.2043	0.8245	1.2101	0.8233
0.50	**1.4371**	**0.6706**	1.4484	0.6680
0.75	1.7055	0.5404	1.7255	0.5358
1.00	2.0318	0.4335	2.0639	0.4285

Table 2
Example 1: normalized mode I SIF in a nonhomogeneous orthotropic plate under fixed grip loading for various effective Poisson's ratios $v = \sqrt{v_{12}v_{21}}$ ($\beta a = 0.5$, $\kappa_0 = 0.5$, $K_0 = \varepsilon_0 \overline{E}^0 \sqrt{\pi a}$; $\overline{E}^0 = E^0/\delta^2$; $E^0 = \sqrt{E^0_{11}E^0_{22}}$) (see Fig. 7)

v	M-integral (present)		Ozturk and Erdogan (1997)	
	$K_I(+a)/K_0$	$K_I(-a)/K_0$	$K_I(+a)/K_0$	$K_I(-a)/K_0$
0.1	1.4300	0.6668	1.4183	0.6647
0.2	1.4334	0.6685	1.4233	0.6676
0.3	**1.4371**	**0.6706**	1.4280	0.6704
0.4	1.4405	0.6731	1.4325	0.6730
0.5	1.4438	0.6751	1.4368	0.6755
0.7	1.4505	0.6785	1.4449	0.6802
0.9	1.4563	0.6827	1.4524	0.6846

Table 3
Example 1: comparison of normalized mode I SIF in a nonhomogeneous orthotropic plate under fixed grip loading for various effective Poisson's ratios ($\beta a = 0.5$, $\kappa_0 = 0.5$, $K_0 = \varepsilon_0 \overline{E}^0 \sqrt{\pi a}$; $\overline{E}^0 = E^0/\delta^2$; $E^0 = \sqrt{E^0_{11}E^0_{22}}$) (see Fig. 7). The J^*_k-integral results were reported by Kim and Paulino (2003a) (cf. Tables 2 and 3)

v	J^*_k-integral		MCC		DCT	
	$K_I(+a)/K_0$	$K_I(-a)/K_0$	$K_I(+a)/K_0$	$K_I(-a)/K_0$	$K_I(+a)/K_0$	$K_I(-a)/K_0$
0.1	1.4451	0.6776	1.4405	0.6630	1.4363	0.6764
0.2	1.4488	0.6802	1.4442	0.6655	1.4405	0.6789
0.3	1.4522	0.6822	1.4480	0.6676	1.4446	0.6814
0.4	1.4559	0.6843	1.4517	0.6697	1.4484	0.6839
0.5	1.4593	0.6864	1.4551	0.6718	1.4517	0.6864
0.7	1.4655	0.6902	1.4618	0.6760	1.4576	0.6902
0.9	1.4718	0.6939	1.4684	0.6802	1.4588	0.6923

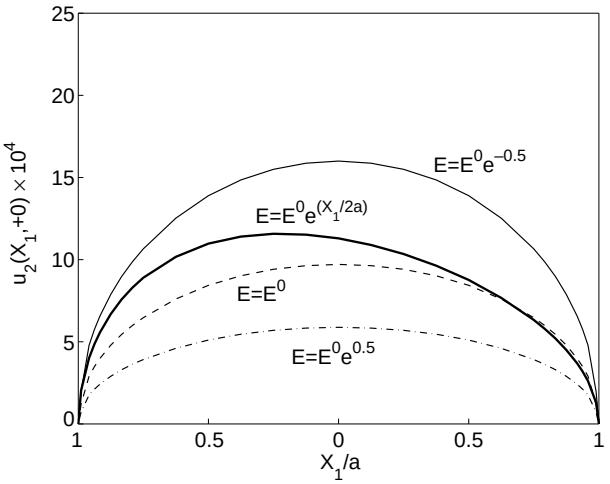

Fig. 8. Example 1: COD in orthotropic FGMs under far-field constant traction considering $\kappa_0 = 0.5$, $v = 0.3$, and $\beta a = 0.5$. The COD for the crack in the FGM is indicated by a thicker line.

The crack opening displacements (CODs) are evaluated for both homogeneous and nonhomogeneous medium considering either fixed-grip loading or far-field constant traction, as shown in Fig. 7(a). Fig. 8

shows the COD in a nonhomogeneous medium ($\beta a = 0.5$) under far-field constant traction with $E = E(X_1) = E^0 e^{X_1/2a}$ ($E^0 = \sqrt{E_{11}^0 E_{22}^0}$) and also in homogeneous materials with $E(-a) = E^0 e^{-0.5}$, $E(0) = E^0$, and $E(a) = E^0 e^{0.5}$. The COD for the right crack tip ($X_1 = a$) in the nonhomogeneous medium is greater than that in the corresponding homogeneous medium with $E(a) = E^0 e^{0.5}$. Thus the mode I SIF K_I in the nonhomogeneous medium is greater than that in the homogeneous medium. Similarly, the mode I SIF (K_I) at the left crack tip ($X_1 = -a$) in the nonhomogeneous medium is lower than that in the corresponding homogeneous medium with $E(-a) = E^0 e^{-0.5}$. The COD for $E = E^0$ serves as a reference curve between those curves for $E = E^0 e^{0.5}$ and $E = E^0 e^{-0.5}$.

Fig. 9 shows the COD in a nonhomogeneous medium under fixed-grip loading with $E = E(X_1) = E^0 e^{X_1/2a}$ and also in homogeneous materials with $E(-a) = E^0 e^{-0.5}$, $E(0) = E^0$, and $E(a) = E^0 e^{0.5}$. Notice that, for the fixed-grip loading, the COD does not depend on material properties in the homogeneous medium. In Eq. (8), the mode SIF K_I for a homogeneous medium under pure mode I loading is given by ($\theta = 180°$):

$$K_I = u_2 \sqrt{\frac{\pi}{2r}} \Big/ \left[\mathrm{Re}\left\{ \frac{\mathrm{i}}{\mu_1 - \mu_2} (\mu_1 q_2 - \mu_2 q_1) \right\} \right], \tag{46}$$

where $q_k = a_{12}\mu_k + a_{22}/\mu_k - a_{26}$ ($k = 1, 2$). The material properties for the three homogeneous materials considered are proportional to one another. In this case, the roots μ_k ($k = 1, 2$) of the characteristic equation (6) are identical. Moreover, for the case where the Cartesian coordinate system coincide with the principal directions of material orthotropy,

$$a_{11} = \frac{1}{E_{11}}, \quad a_{12} = \frac{-\nu_{12}}{E_{11}}, \quad a_{16} = 0.$$

Thus, with the same crack surface displacement u_2 and Poisson's ratio ν_{12}, the mode I SIF K_I is proportional to E_{11}, as illustrated by Table 4. By comparison of the solution of a nonhomogeneous medium with that of a homogeneous medium having the material properties at the right crack tip ($X_1 = a$), the COD in the nonhomogeneous medium is smaller than that in the corresponding homogeneous medium with $E(a) = E^0 e^{0.5}$, and thus the SIF (K_I) in the nonhomogeneous medium is lower than that for the corresponding

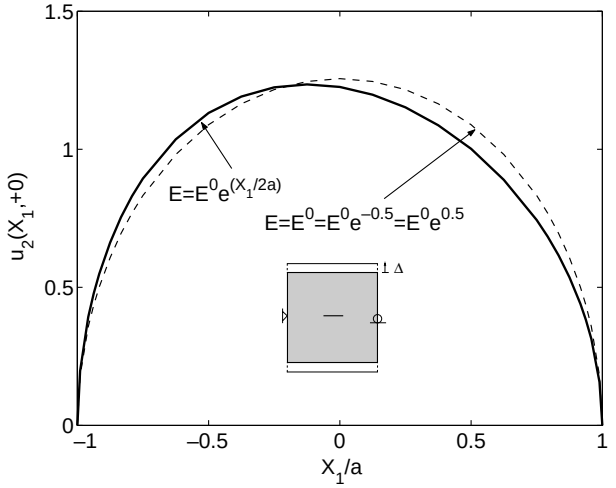

Fig. 9. Example 1: COD u_2 in orthotropic FGMs under fixed-grip loading considering $\kappa_0 = 0.5$, $\nu = 0.3$, and $\beta a = 0.5$. The COD for the crack in the FGM is indicated by a thicker line.

Table 4
Example 1: homogeneous orthotropic material with properties sampled at the crack tips ($X_1 = \pm 1.0$) and at the mid-point of the crack ($X_1 = 0$) in the corresponding FGM (see Eq. (45)). For all the cases, $\kappa_0 = 0.5$, $K_0 = \varepsilon_0 \overline{E}^0 \sqrt{\pi a}$; $\overline{E}^0 = E^0/\delta^2$; $E^0 = \sqrt{E_{11}^0 E_{22}^0}$. Also, notice that $E = E^0 e^{\beta X_1}$. The superscript in K_I^1 indicates case 1

Parameter	Case		
	1	2	3
E_{11}	$E_{11}^0 e^{-\beta}$	E_{11}^0	$E_{11}^0 e^{\beta}$
K_I/K_0	K_I^1/K_0	$K_I^1 e^{\beta}/K_0$	$K_I^1 e^{2\beta}/K_0$
K_I/K_0 (numerical)	0.6046	0.9969	1.6436

homogeneous medium. Similarly, the mode I SIF (K_I) at the left crack tip ($X_1 = -a$) in the nonhomogeneous medium is greater than that in the corresponding homogeneous medium with $E(-a) = E^0 e^{-0.5}$.

5.2. Plate with a crack perpendicular to material gradation

Fig. 10(a) and (b) show a crack of length $2a$ located in a finite two-dimensional plate under remote uniform tension loading for two different boundary conditions. These boundary conditions are prescribed such that, for Fig. 10(a), $u_1 = 0$ along the left and right edges, and $u_2 = 0$ for the node in the middle of left edge; while for Fig. 10(b), $u_1 = 0$ for the left corner node of the bottom edge and $u_2 = 0$ along the bottom edge. The finite element mesh configurations are the same as in the previous example (see Fig. 7(b) and (c)). The applied load corresponds to $\sigma_{22}(X_1, \pm L) = \pm\sigma = \pm 1.0$ for the BC in Fig. 10(a) and $\sigma_{22}(X_1, L) = \sigma = 1.0$ for the BC in Fig. 10(b).

The variations of E_{11}, E_{22}, and G_{12} are exponential functions of X_2 and are *proportional* to one another, while the Poisson's ratio ν_{12} is constant. The following data were used for the FEM analysis:

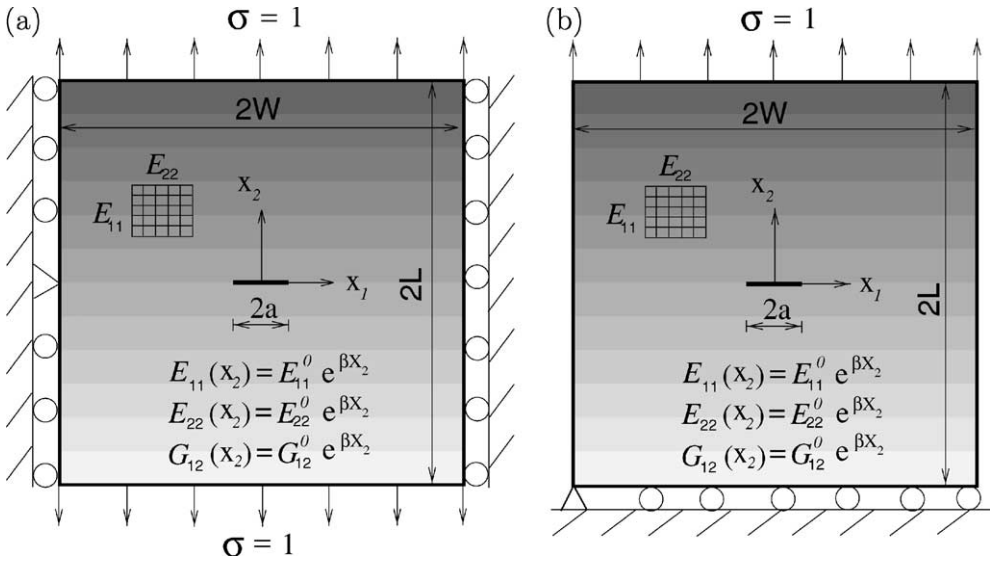

Fig. 10. Example 2: plate with a center crack perpendicular to the material gradation: (a) first set of BCs; (b) second set of BCs.

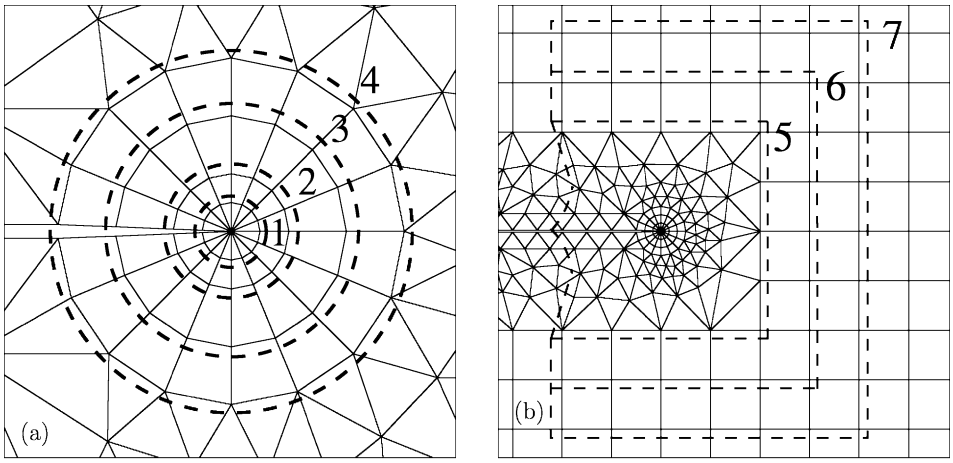

Fig. 11. Example 2: contours used to evaluate the J-integral: (a) contours 1, 2, 3, and 4; (b) contours 5, 6, and 7.

$a/W = 0.1, \quad L/W = 1.0,$

$E_{11}(X_2) = E_{11}^0 e^{\beta X_2}, \quad E_{22}(X_2) = E_{22}^0 e^{\beta X_2}, \quad G_{12}(X_2) = G_{12}^0 e^{\beta X_2},$

dimensionless nonhomogeneity parameter : $\beta a = (0.0\text{–}0.5)$,

$\delta^4 = E_{11}/E_{22} = (0.25, 0.5, 1.0, 3.0, 10.0)$,

$\kappa_0 = (-0.25, 0.0, 0.5, 1.0, 2.0, 5.0), \quad \nu = 0.30,$

plane stress, 2×2 Gauss quadrature.

Fig. 11(a) and (b) show seven contours used for evaluating the J-integral considering $\delta^4 = 10$, $\kappa_0 = 5.0$, $\nu = 0.3$, and $\beta a = 0.5$. Figs. 12 and 13 show the effect of the incompatible term (see Eq. (27)) on the convergence of the J-integral obtained from Eq. (35) considering the two sets of BCs, respectively. Notice

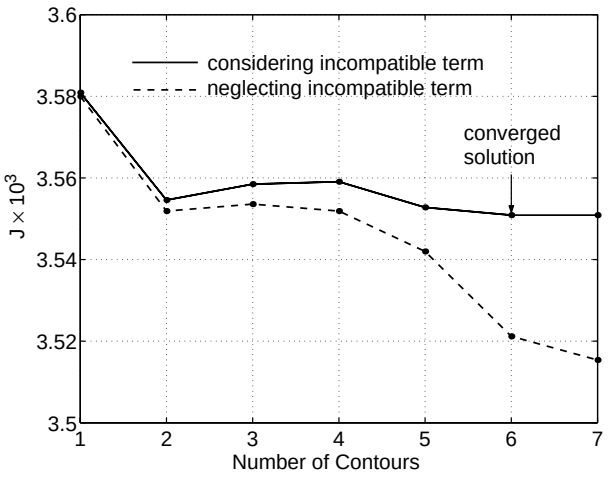

Fig. 12. Example 2: effect of the "incompatible term" on the path-independence of the J-integral considering the first set of BCs. The region associated with each contour is illustrated by Fig. 11.

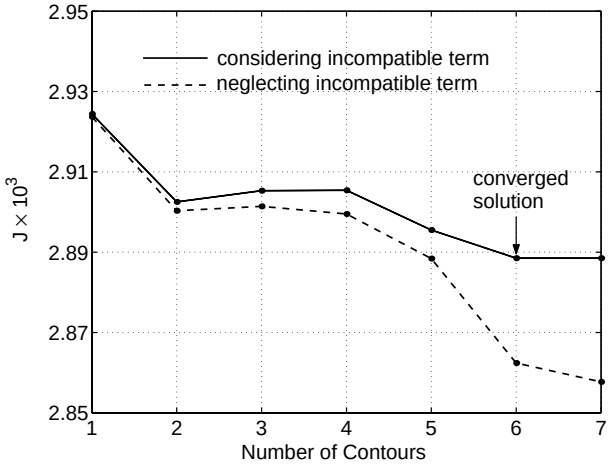

Fig. 13. Example 2: effect of the "incompatible term" on the path-independence of the J-integral considering the second set of BCs. The region associated with each contour is illustrated by Fig. 11.

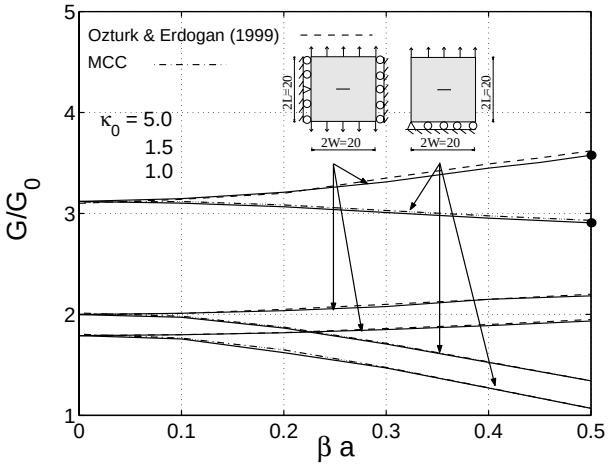

Fig. 14. Example 2: normalized strain energy release rate versus the nonhomogeneity parameter βa and the shear parameter κ_0 considering uniformly applied tension ($\sigma_{22}(X_1, \pm L) = \pm\sigma$ for the first set of BCs, and $\sigma_{22}(X_1, L) = \sigma$ for the second set of BCs) and $\delta^4 = 10.0, \nu = 0.3, \mathscr{G}_0 = \pi\sigma^2 a/E^0$. The dashed lines indicate the results reported by Ozturk and Erdogan (1999), and the dash-dotted lines indicate the results obtained by means of the MCC method. The solid lines indicate the results by means of the present M-integral considering the two BCs, and the two bullets at $\beta a = 0.5$ indicate the converged solutions for J considering $\kappa_0 = 5.0$ as shown in Figs. 12 and 13, respectively.

that J is obtained after evaluation of SIFs (see Eq. (35)). As the contours become larger, the solution converges when the incompatible term is considered, however, it diverges if such term is neglected. Fig. 14 shows strain energy release rates $\mathscr{G}/\mathscr{G}_0$ in a nonhomogeneous orthotropic plate under uniform tension for two different boundary conditions for a fixed stiffness ratio $\delta^4 = 10$ and constant Poisson's ratio $\nu = 0.3$ with varying material nonhomogeneity βa and κ_0. This figure clearly indicates that the boundary conditions have a significant influence in strain energy release rates (and SIFs). For the first set of BCs (see Fig. 10(a)), the FEM results agree with the strain energy release rates ($\mathscr{G}/\mathscr{G}_0$) obtained by Ozturk and Erdogan (1999). The strain energy release rates $\mathscr{G}/\mathscr{G}_0$ monotonically increase with κ_0 and βa. However, for the second set of

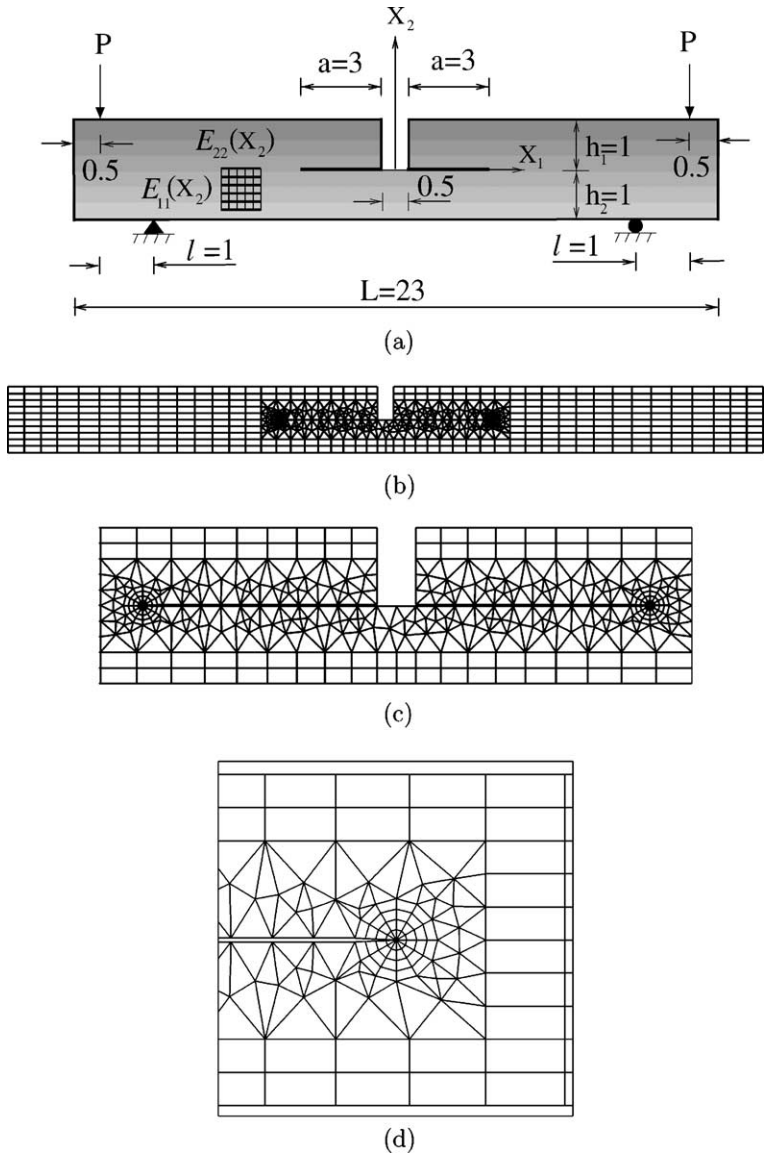

Fig. 15. Example 3: four-point bending specimen: (a) geometry and BCs; (b) complete finite element mesh; (c) mesh detail using 12 sectors (S12) and four rings (R4) around crack tips; (d) zoom of the right crack tip.

BCs (see Fig. 10(b)), the present results agree with the strain energy release rates ($\mathscr{G}/\mathscr{G}_0$) obtained by the MCC, and the FEM results are significantly different from those for the previous BCs. Notice that the two bullets along the line $\beta a = 0.5$ indicate energy release rates which are the converged solutions for J as shown in Figs. 12 and 13. The FEM results for various δ^4 and κ_0 obtained by the interaction integral compare well to those obtained by the path-independent J_k^*-integral (Kim and Paulino, 2003a), which are not presented in this paper. Further numerical results investigating the effect of boundary conditions, Poisson's ratio, and plate size on the strain energy release rates considering the two BCs of Fig. 10 can be found in the papers by Kim and Paulino (2002c, 2003a).

5.3. Four-point bending specimen

Gu and Asaro (1997) investigated the effect of material orthotropy on mixed-mode SIFs in FGMs considering a four-point bending specimen with exponentially varying Young's moduli, shear modulus, and Poisson's ratio. Fig. 15(a) shows the four-point bending specimen geometry and BCs, Fig. 15(b) shows the complete FEM mesh configuration, Fig. 15(c) shows a mesh detail around the crack, and Fig. 15(d) shows a zoom of the right crack tip. The point loads of magnitude P are applied at the nodes $(X_1, X_2) = (\pm 11, 1.0)$. The displacement boundary conditions are prescribed such that $(u_1, u_2) = (0, 0)$ for the node at $(X_1, X_2) = (-10, -1.0)$ and $u_2 = 0$ for the node at $(X_1, X_2) = (10, -1.0)$. Young's moduli, shear modulus, and Poisson's ratios are exponential functions of X_2 given by

$$\begin{aligned} &E_{11}(X_2) = E_{11}^0 \mathrm{e}^{\beta X_2}, \quad E_{22}(X_2) = E_{22}^0 \mathrm{e}^{\beta X_2}; \\ &\nu_{12}(X_2) = \nu_{12}^0 (1 + \epsilon X_2) \mathrm{e}^{\beta X_2}, \quad \nu_{21}(X_2) = \nu_{21}^0 (1 + \epsilon X_2) \mathrm{e}^{\beta X_2}; \\ &G_{12}(X_2) = E_{22}(X_2) / [2(\sqrt{\lambda} + \nu_{21}(X_2))]; \quad \lambda = E_{22}(X_2)/E_{11}(X_2); \end{aligned} \tag{47}$$

respectively. Notice that $\lambda = 1/\delta^4$ (see Eq. (42)). The mesh discretization consists of 625 Q8, 203 T6, and 24 T6qp elements, with a total of 852 elements and 2319 nodes. The following data were used for the FEM analysis:

$$\begin{aligned} &\text{plane stress, } \ 2 \times 2 \text{ Gauss quadrature,} \\ &a = 3.0, \quad h_1/h_2 = 1.0, \quad \epsilon = -0.9, \quad P = 1.0. \end{aligned} \tag{48}$$

Figs. 16 and 17 show comparison of the SIF $|K|h_1^{3/2}/Pl$ with $|K| = \sqrt{K_{\mathrm{I}}^2 + K_{\mathrm{II}}^2}$, and the phase angle $\psi = \tan^{-1}(K_{\mathrm{II}}/K_{\mathrm{I}})$, respectively, obtained by the interaction integral method with those reported by Gu and Asaro (1997). There is quite good agreement between the two solutions, although Gu and Asaro (1997) did not provide geometry information. Notice that as βh_1 increases, both the SIF and the phase angle ψ increase, and the material orthotropy (measured by $\lambda = E_{22}/E_{11}$) shows significant influence on the results. Moreover, for a fixed βh_1, as λ increases the SIF increases, however, the phase angle decreases.

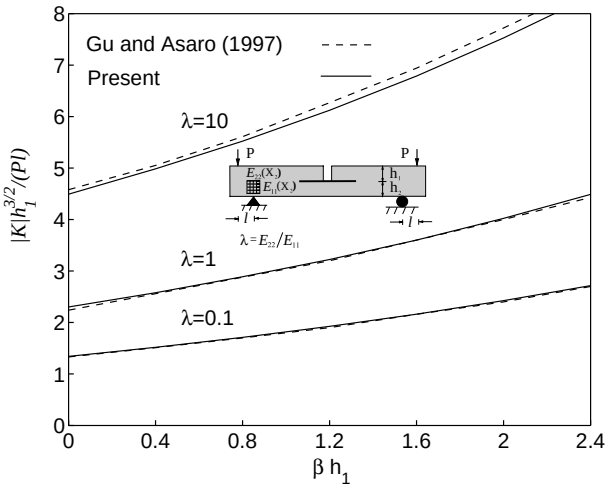

Fig. 16. Example 3: the normalized norm of mixed-mode SIFs $|K|h_1^{3/2}/Pl$ for a four-point bending specimen. The parameter $\lambda = E_{22}/E_{11}$.

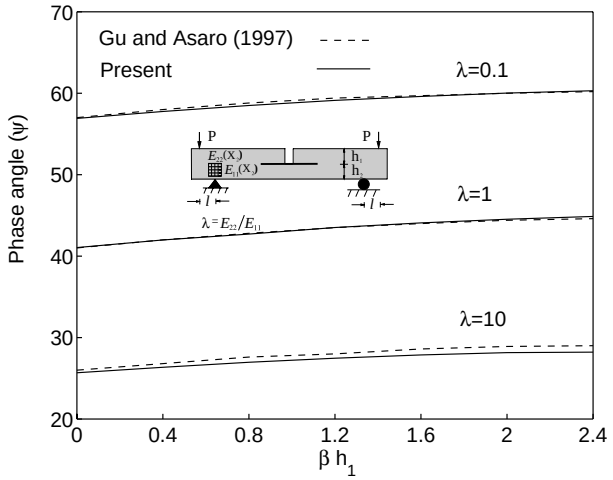

Fig. 17. Example 3: the phase angle $\psi = \tan^{-1}(K_I/K_{II})$ for a four-point bending specimen. The parameter $\lambda = E_{22}/E_{11}$.

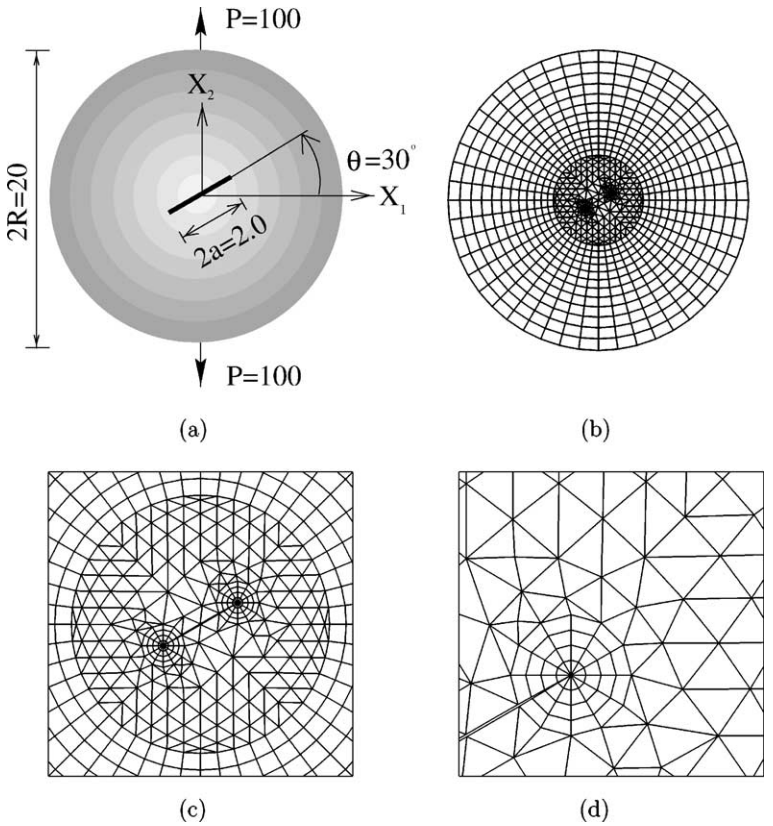

Fig. 18. Example 4: a circular disk; (a) geometry and BCs for an inclined center crack; (b) the complete mesh configuration; (c) mesh detail displaying 12 sectors (S12) and four rings (R4) around the crack tips; (d) zoom of the right crack tip.

5.4. Disk with an inclined center crack

Fig. 18(a) shows a circular disk with a center crack inclined by $\theta = 30°$, Fig. 18(b) shows the complete mesh configuration, Fig. 18(c) shows the mesh detail around the crack, and Fig. 18(d) shows a zoom of the right crack tip. A point load is applied to the top and bottom nodes, i.e. $P(0, \pm 10) = \pm 100$. The displacement boundary conditions are prescribed such that $(u_1, u_2) = (0, 0)$ for the node at $(X_1, X_2) = (-10, 0)$ and $u_2 = 0$ for the node at $(X_1, X_2) = (10, 0)$. Three different exponential material gradations with respect to the radial (r) and Cartesian directions (X_1) and (X_2) are considered as given below:

$$\begin{aligned} &E_{11}(r) = E_{11}^0 e^{\alpha r}, \quad E_{22}(r) = E_{22}^0 e^{\beta r}, \quad G_{12}(r) = G_{12}^0 e^{\gamma r}; \quad r = \sqrt{X_1^2 + X_2^2}, \\ &E_{11}(X_1) = E_{11}^0 e^{\alpha |X_1|}, \quad E_{22}(X_1) = E_{22}^0 e^{\beta |X_1|}, \quad G_{12}(X_1) = G_{12}^0 e^{\gamma |X_1|}, \\ &E_{11}(X_2) = E_{11}^0 e^{\alpha |X_2|}, \quad E_{22}(X_2) = E_{22}^0 e^{\beta |X_2|}, \quad G_{12}(X_2) = G_{12}^0 e^{\gamma |X_2|}. \end{aligned} \tag{49}$$

The mesh discretization consists of 747 Q8, 228 T6, and 24 T6qp elements, with a total of 999 elements and 2712 nodes. The following data were used for the FEM analysis:

plane stress, 2×2 Gauss quadrature,

$a/R = 0.1$,

Isotropic case:

$E = 1.0, \quad \nu = 0.3$,

Orthotropic case:

$$E_{11}^0 = 0.1, \quad E_{22}^0 = 1.0, \quad G_{12}^0 = 0.5, \quad \nu_{12} = 0.03,$$
$$E_{11}^0 = 1.0, \quad E_{22}^0 = 1.0, \quad G_{12}^0 = 0.5, \quad \nu_{12} = 0.03.$$

Table 5 shows the FEM results for SIFs for the isotropic and orthotropic cases considering various material nonhomogeneity parameters βa for an inclined center crack in a circular disk with radial gradation and proportional material variation ($\alpha a = \beta a = \gamma a$). It also compares the present results with those obtained using the MCC (Kim and Paulino, 2002c) and shows good agreement between the two methods. Notice that, as the nonhomogeneity parameter βa increases, the SIFs decrease for both isotropic and orthotropic cases. Fig. 19 shows the crack opening profile representing high mode-mixity for the orthotropic FGM case considering the radial gradation and proportional material variation ($\alpha a = \beta a = \gamma a = 0.5$). To illustrate the effect of radial gradation on a single property (nonproportional material variation), Table 6 shows the FEM results for SIFs considering three different variations: E_{11} (Cases 1 and 4: $\alpha a = 0.1$, $\beta a = \gamma a = 0.0$), E_{22} (Cases 2 and 5: $\beta a = 0.1$, $\alpha a = \gamma a = 0.0$), and G_{12} (Cases 3 and 6: $\gamma a = 0.1$,

Table 5
Example 4: FEM results for SIFs for an inclined center crack in a circular disk considering radial gradation and $\alpha a = \beta a = \gamma a$: $E_{11}^0 = 0.1$; $E_{22}^0 = 1.0$; $G_{12}^0 = 0.5$; $\nu_{12} = 0.03$ for orthotropic case, and $E = 1.0$; $\nu = 0.3$ for isotropic case (see Fig. 18)

βa	Isotropic				Orthotropic			
	M-integral		MCC		M-integral		MCC	
	K_I	K_{II}	K_I	K_{II}	K_I	K_{II}	K_I	K_{II}
−0.50	22.91	15.19	22.54	14.76	29.72	18.89	29.22	18.56
−0.25	17.53	13.21	17.37	12.92	23.37	15.38	23.16	15.21
0.00	11.47	9.730	11.45	9.596	16.75	11.38	16.73	11.33
0.25	5.862	5.651	5.898	5.602	10.51	7.302	10.57	7.318
0.50	2.205	2.417	2.236	2.412	5.380	3.813	5.459	3.847

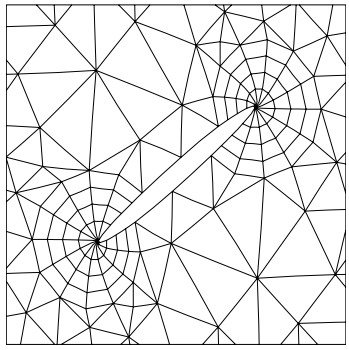

Fig. 19. Example 4: crack opening profile considering radial gradation, $E_{11}^0 = 0.1$; $E_{22}^0 = 1.0$; $G_{12}^0 = 0.5$; $\nu_{12} = 0.03$, and $\alpha a = \beta a = \gamma a = 0.5$.

Table 6
Example 4: FEM results for SIFs for an inclined center crack in a circular disk considering radial gradation and $E_{11}^0 = 0.1$ or 1.0; $E_{22}^0 = 1.0$; $G_{12}^0 = 0.5$; $\nu_{12} = 0.03$ (see Fig. 18)

Case	E_{11}^0	Nonhomogeneity parameters	M-integral		MCC	
			K_{I}	K_{II}	K_{I}	K_{II}
1	0.1	$\alpha a = 0.1$, $\beta a = \gamma a = 0.0$	15.46	10.46	15.45	10.42
2	0.1	$\beta a = 0.1$, $\alpha a = \gamma a = 0.0$	17.09	11.54	17.08	11.50
3	0.1	$\gamma a = 0.1$, $\alpha a = \beta a = 0.0$	16.75	11.38	16.73	11.33
4	1.0	$\alpha a = 0.1$, $\beta a = \gamma a = 0.0$	10.68	8.907	10.67	8.775
5	1.0	$\beta a = 0.1$, $\alpha a = \gamma a = 0.0$	11.85	9.904	11.86	9.766
6	1.0	$\gamma a = 0.1$, $\alpha a = \beta a = 0.0$	9.641	9.079	9.633	8.943

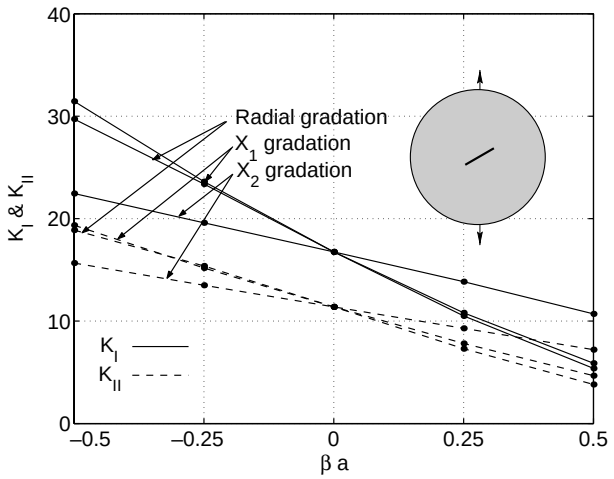

Fig. 20. Example 4: effect of gradation direction on SIFs for an orthotropic and exponentially graded disk. The following cases are considered: $E_{11} = E_{11}^0 e^{\alpha r}$, $E_{11} = E_{11}^0 e^{\alpha |X_1|}$, and $E_{11} = E_{11}^0 e^{\alpha |X_2|}$. Analogous expressions are also adopted for E_{22} and G_{12}.

$\alpha a = \beta a = 0.0$). There is very good agreement between the M-integral and the MCC. Fig. 20 shows the effect of gradation direction (radial versus Cartesian) on SIFs for the orthotropic FGM case considering proportional material gradation ($\alpha a = \beta a = \gamma a$). As the βa increases, mixed-mode SIFs decrease in a

monotonic fashion. The SIFs evaluated for the radial gradation are similar to those evaluated for the Cartesian gradation of X_1, but differs from those for the Cartesian gradation of X_2.

5.5. Plate with a curved crack

Muskhelishvili (1953) used conformal mapping and provided the exact solutions for SIFs of a curved crack in a homogeneous medium under far-field traction, according to the scheme shown in Fig. 21. The exact solutions for SIFs are given by

$$\begin{aligned} K_{\mathrm{I}} &= \frac{\sigma\sqrt{\pi R\sin\theta}}{2}\left[F(\theta)\cos\frac{\theta}{2}+\sin 2\omega\sin^3\frac{\theta}{2}+\cos\left(2\omega-\frac{3\theta}{2}\right)\right], \\ K_{\mathrm{II}} &= \frac{\sigma\sqrt{\pi R\sin\theta}}{2}\left[F(\theta)\sin\frac{\theta}{2}-\sin 2\omega\sin^2\frac{\theta}{2}\cos\frac{\theta}{2}-\sin\left(2\omega-\frac{3\theta}{2}\right)\right], \end{aligned} \tag{50}$$

where

$$F(\theta)=\frac{1-\cos 2\omega\sin^2(\theta/2)\cos^2(\theta/2)}{1+\sin^2(\theta/2)},$$

in which ω indicates the angle of the direction of applied traction σ with respect to the horizontal line, and K_{I} and K_{II} are the SIFs at the top crack tip (tip A). The mode I SIF at the bottom crack tip (tip B) is the same as K_{I} in Eq. (50), however, the mode II SIF changes sign. Our numerical solution (M-integral) will be tested against these theoretical (reference) solutions.

Fig. 22(a) and (b) show a circular-shaped crack located in a finite two-dimensional plate under remote uniform tension loading for two different boundary conditions. These boundary conditions are prescribed such that, for the first set of BCs (Fig. 22(a)), $u_1 = u_2 = 0$ for the node in the middle of the left edge, and $u_2 = 0$ for the node in the middle of the right edge; while for the second set of BCs (Fig. 22(b)), $u_1 = u_2 = 0$ for the node in the middle of the bottom edge, and $u_1 = 0$ for the node in the middle of the top edge. Fig. 22(c) shows the complete finite element mesh configuration, and Fig. 22(d) shows a mesh detail using 12 sectors (S12) and five rings (R5) around the crack tips. The applied load corresponds to $\sigma_{22}(X_1, \pm L) = \pm\sigma = \pm 1.0$ for the BC in Fig. 22(a) and $\sigma_{11}(\pm W, X_2) = \pm\sigma = \pm 1.0$ for the BC in Fig. 22(b). The mesh discretization consists of 1691 Q8, 184 T6, and 24 T6qp elements, with a total of 1875 elements and 5608 nodes. The following data were used in the FEM analyses:

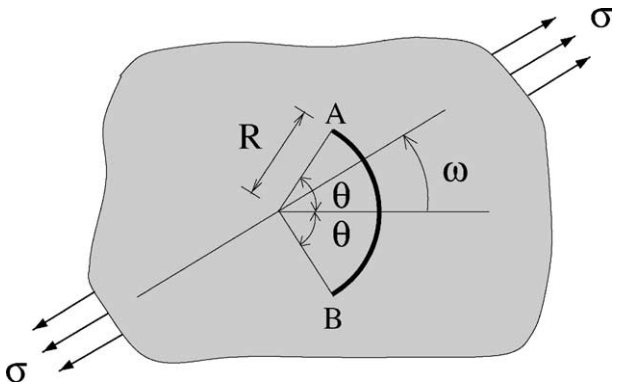

Fig. 21. Example 5: a curved crack (circular) under far-field traction.

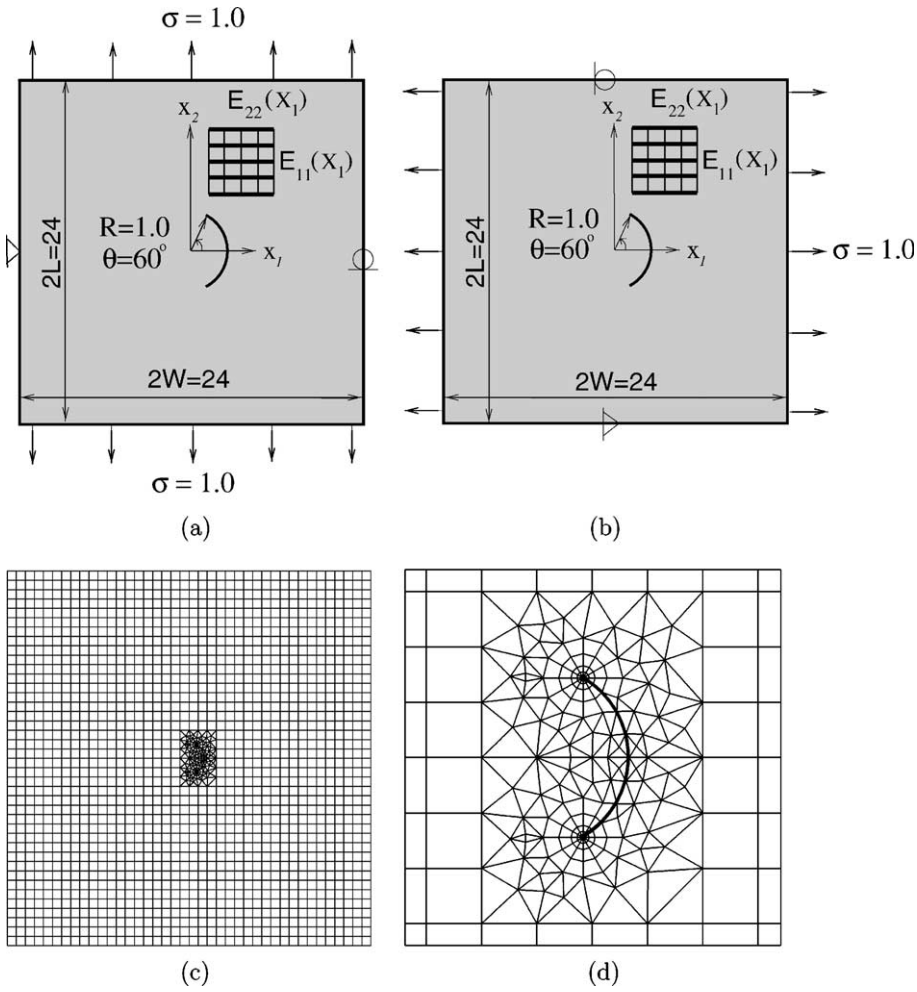

Fig. 22. Example 5: plate with a circular-shaped crack: (a) geometry and BCs (first set of BCs); (b) geometry and BCs (second set of BCs); (c) complete finite element mesh; (d) mesh detail with 12 sectors (S12) and 5 rings (R5) around the crack tip – the thick line indicates the crack faces.

plane stress, 2×2 Gauss quadrature,

$R = 1.0, \quad L/W = 1.0,$

Isotropic case (*homogeneous*):

$E = 1.0, \quad v = 0.3,$

Orthotropic case:

$$E_{11}(X_1) = E^0_{11}e^{\beta X_1}, \quad E_{22}(X_1) = E^0_{22}e^{\beta X_1}, \quad G_{12}(X_1) = G^0_{12}e^{\beta X_1},$$
$$E_{11}(X_2) = E^0_{11}e^{\beta X_2}, E_{22}(X_2) = E^0_{22}e^{\beta X_2}, \quad G_{12}(X_2) = G^0_{12}e^{\beta X_2},$$
$$E^0_{11} = 1.0, \quad E^0_{22} = 0.5, \quad G^0_{12} = 0.25, \quad v_{12} = 0.3,$$

dimensionless nonhomogeneity parameter : $\beta R = (0.0, 0.1)$.

Table 7
Example 5: FEM results for SIFs for a semi-circular crack. Case 1: first set of BCs—Fig. 22(a); Case 2: second set of BCs—Fig. 22(b). The exact solution for homogeneous isotropic materials was reported by Muskhelishvili (1953)

Crack tip	Case	Material	βR	Gradation direction	M-integral		MCC		Exact	
					K_I	K_{II}	K_I	K_{II}	K_I	K_{II}
Top	1	Iso	0.0	–	0.6872	−0.4314	0.6765	−0.4303	0.6785	−0.4330
		Ortho	0.0	–	0.6868	−0.4362	0.6853	−0.4321	–	–
			0.1	X_1	0.8240	−0.3718	0.8218	−0.3678	–	–
				X_2	0.6602	−0.4498	0.6596	−0.4451	–	–
	2	Iso	0.0	–	0.4690	1.0890	0.4692	1.0890	0.4643	1.0928
		Ortho	0.0	–	0.5059	1.0470	0.5053	1.0412	–	–
			0.1	X_1	0.5131	1.0489	0.5125	1.0425	–	–
				X_2	0.6160	1.0771	0.6159	1.0734	–	–
Bottom	1	Ortho	0.1	X_2	0.6739	0.4351	0.6700	0.4306	–	–
	2	Ortho	0.1	X_2	0.5341	−1.0692	0.5338	−1.0628	–	–

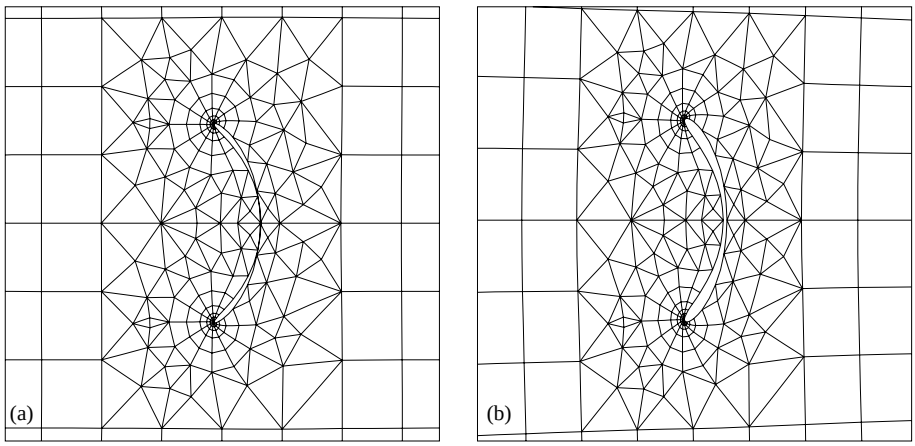

Fig. 23. Example 5: curved crack surface displacement profile (deformed shape) considering the first set of BCs: (a) isotropic homogeneous case; (b) orthotropic FGM with gradation along the X_1 direction.

Table 7 shows FEM results for SIFs for both the top and bottom crack tips obtained by means of the interaction integral for a semi-circular crack considering the two sets of boundary conditions and the two choices of gradation directions, i.e. X_1 and X_2. It also compares the present results with the available reference solutions of Muskhelishvili (1953) for the homogeneous isotropic case. In this latter case, the numerical solutions are obtained as a particular case of the general formulation for nonhomogeneous orthotropic materials. The calculated SIFs agree well with the reference solutions (Muskhelishvili, 1953). For material gradation along the direction X_1, the mode II SIF at the bottom crack tip changes sign because of symmetry, however, for material gradation along the X_2 direction, both mode I and mode II SIFs change in magnitude and sign.

Fig. 23(a) and (b) show curved crack surface displacement profile considering the isotropic homogeneous case and the orthotropic FGM case with gradation along the X_1 direction, respectively, for the first set of BCs (see Fig. 22(a)). Notice that the curved crack geometry naturally creates mode-mixity which is observed around crack-tip elements. Moreover, the symmetry of crack opening profiles exists with respect to

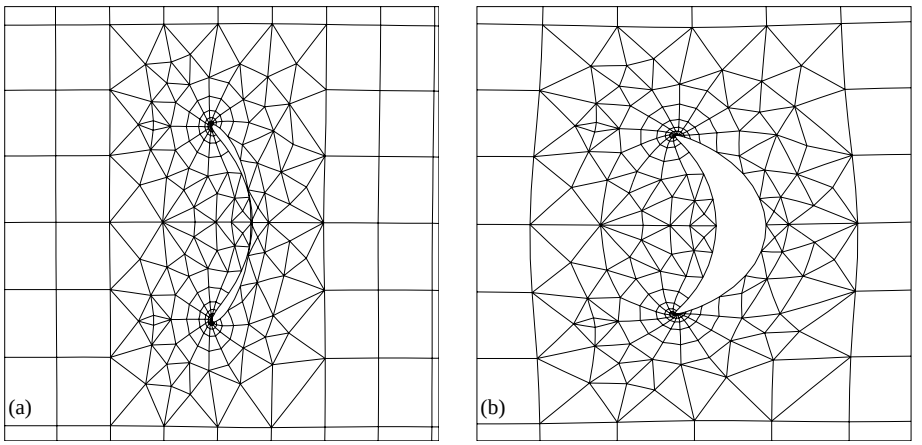

Fig. 24. Example 5: curved crack surface displacement profile (deformed shape) considering gradation along the X_2 direction in orthotropic FGMs: (a) first set of BCs; (b) second set of BCs.

the Cartesian direction X_1 for this case, i.e. the homogeneous case and FGM case with gradation of X_1. The crack faces interpenetrate for the isotropic homogeneous case, while this behavior does not occur for the orthotropic FGM case. Fig. 24(a) and (b) show curved crack surface displacement profile considering the orthotropic FGM case with gradation of X_2 for the first and second set of BCs, respectively. We observe that the interpenetration of the crack faces is also observed for the orthotropic FGM case with gradation of X_2 using the first set of BCs. As expected, the symmetry of crack opening profiles is naturally lost for the FGM with gradation along X_2 direction (refer to SIFs in Table 7).

5.6. Strip with an edge crack

Fig. 25(a) shows an edge crack of length "a" in a graded plate, and Fig. 25(b) shows the complete mesh discretization using 12 sectors (S12) and 4 rings (R4) of elements around the crack tip. Fig. 25(c)–(e) illustrate the three considered types of hyperbolic-tangent material gradation with respect to the crack tip: reference configuration, translation to the left, and translation to the right, respectively. The fixed-grip displacement loading results in a uniform strain $\varepsilon_{22}(X_1, X_2) = \varepsilon_0$ in a corresponding uncracked structure. The displacement boundary condition is prescribed such that $u_2 = 0$ along the lower edge and $u_1 = 0$ for the node at the left hand side.

Young's moduli and shear modulus are hyperbolic-tangent functions with respect to the global (X_1, X_2) Cartesian coordinates as follows:

$$\begin{aligned} E_{11}(X_1) &= \frac{E_{11}^- + E_{11}^+}{2} + \frac{E_{11}^- - E_{11}^+}{2}\tanh[\alpha(X_1 + d)], \\ E_{22}(X_1) &= \frac{E_{22}^- + E_{22}^+}{2} + \frac{E_{22}^- - E_{22}^+}{2}\tanh[\beta(X_1 + d)], \\ G_{12}(X_1) &= \frac{G_{12}^- + G_{12}^+}{2} + \frac{G_{12}^- - G_{12}^+}{2}\tanh[\gamma(X_1 + d)], \end{aligned} \tag{51}$$

where d is a constant for translation. In this example, the Poisson's ratio v_{12} is taken as constant. The mesh discretization consists of 208 Q8, 37 T6, and 12 T6qp elements, with a total of 257 elements and 1001 nodes. The following data were used for the FEM analysis:

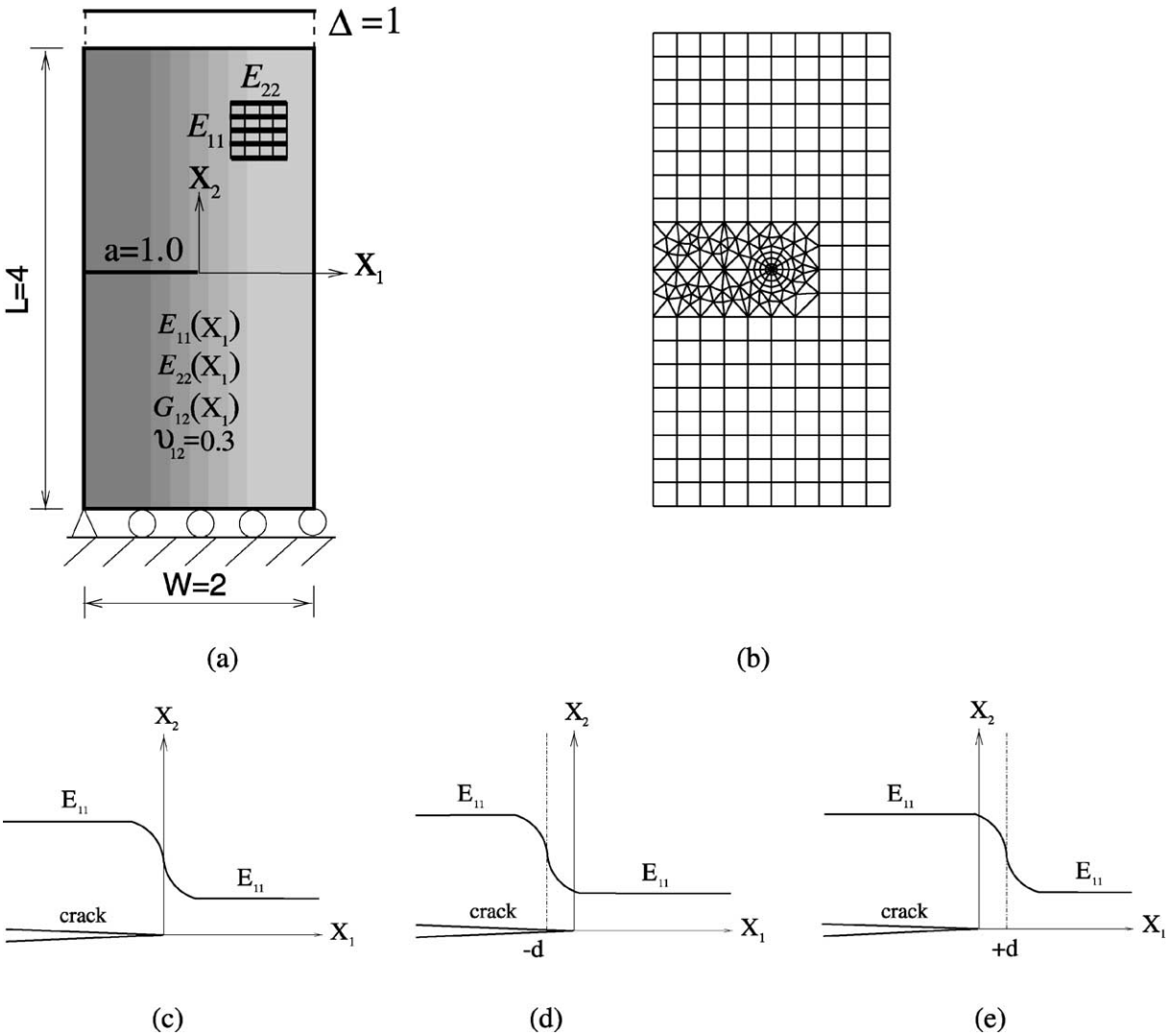

Fig. 25. Example 6: strip with an edge crack in hyperbolic-tangent materials: (a) geometry and BCs; (b) complete finite element mesh with 12 sectors (S12) and four rings (R4) around the crack tip; (c) reference configuration ($d = 0.0$); (d) translation of material gradation to the left ($d = +0.5$); (e) translation of material gradation to the right ($d = -0.5$).

plane stress, 2×2 Gauss quadrature,

$a/W = 0.5, \quad L/W = 2.0, \quad \varepsilon_0 = 0.25,$

$d = (-0.5 \text{ to } 0.5), \quad \nu_{12} = 0.3,$

Case 1: Proportional material variation (see Fig. 26)

$\alpha a = \beta a = \gamma a = 15.0,$

$(E_{11}^-, E_{11}^+) = (1.00, 3.00), \quad (E_{22}^-, E_{22}^+) = (1.25, 2.75), \quad (G_{12}^-, G_{12}^+) = (1.50, 2.50),$

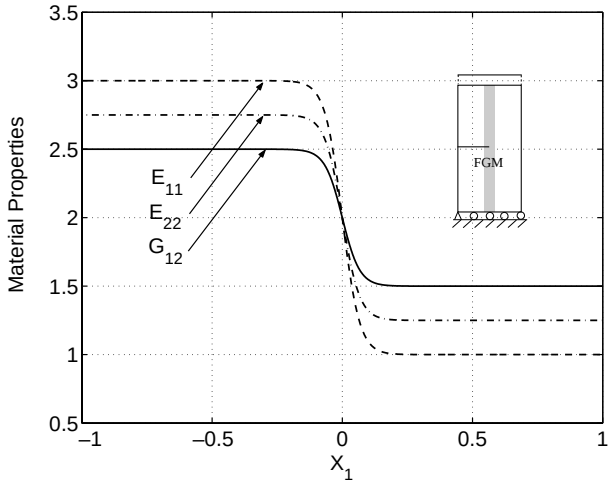

Fig. 26. Example 6: *proportional* variation of material properties (Case 1).

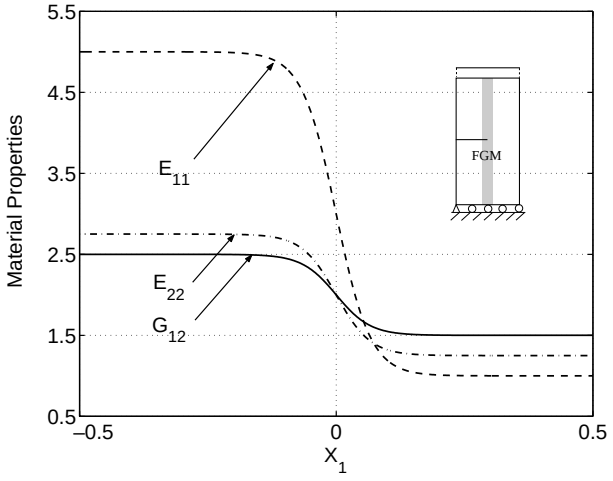

Fig. 27. Example 6: *proportional* variation of material properties (Case 2).

Case 2: Proportional material variation (see Fig. 27)

$$\alpha a = \beta a = \gamma a = 15.0,$$
$$(E_{11}^{-}, E_{11}^{+}) = (1.00, 5.00), \quad (E_{22}^{-}, E_{22}^{+}) = (1.25, 2.75), \quad (G_{12}^{-}, G_{12}^{+}) = (1.50, 2.50),$$

Case 3: Nonproportional material variation (see Fig. 28)

$$\begin{aligned} &\alpha a = 4.0, \quad \beta a = 2.0, \quad \gamma a = 1.0, \\ &(E_{11}^{-}, \quad E_{11}^{+}) = (E_{22}^{-}, \quad E_{22}^{+}) = (G_{12}^{-}, \quad G_{12}^{+}) = (1.00, 3.00). \end{aligned} \tag{52}$$

Table 8 shows the present FEM results for mode I SIF (K_I) for various translation factors of hyperbolic-tangent material variation considering three particular cases of material variations. For proportional

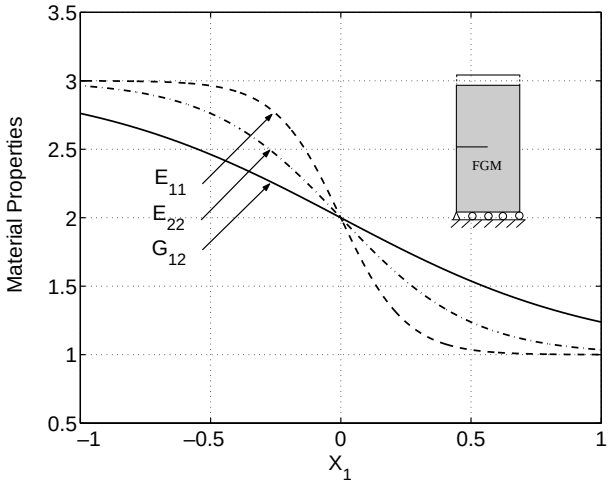

Fig. 28. Example 6: *nonproportional* variation of material properties (Case 3).

Table 8
Example 6: FEM results for mode I SIF (K_I) for an edge crack with translation of hyperbolic-tangent material variation. Case 1: proportional material variation (Fig. 26); Case 2: proportional material variation (Fig. 27); Case 3: Nonproportional material variation (Fig. 28)

d	M-integral			MCC		
	Case 1	Case 2	Case 3	Case 1	Case 2	Case 3
−0.5	1.158	1.214	1.190	1.153	1.187	1.180
−0.4	1.163	1.215	1.165	1.155	1.190	1.150
−0.3	1.173	1.241	1.129	1.160	1.195	1.109
−0.2	1.189	1.252	1.081	1.173	1.208	1.055
−0.1	1.217	1.287	1.016	1.181	1.216	0.988
0	1.049	1.099	0.935	0.974	0.994	0.910
0.1	0.697	0.714	0.846	0.683	0.686	0.828
0.2	0.614	0.619	0.759	0.612	0.614	0.751
0.3	0.585	0.587	0.684	0.584	0.586	0.682
0.4	0.567	0.568	0.623	0.566	0.567	0.623
0.5	0.554	0.555	0.574	0.554	0.554	0.575

material variations (Cases 1 and 2), the mode I SIF increases with the translation factor d for the range between −0.5 and −0.1, however, it decreases as d increases further. For nonproportional material variations (Case 3), such behavior is not observed, and the mode I SIF decreases as the translation factor d increases. Moreover, the crack tip location shows significant influence on SIFs for all the three cases of hyperbolic-tangent material variation. For all the three cases investigated, the M-integral results compare reasonably well with those provided by the MCC method.

6. Conclusions and extensions

This paper presents an accurate scheme for evaluating mixed-mode SIFs by means of the interaction integral (M-integral) method considering arbitrarily oriented straight and curved cracks in two-dimensional (2D) elastic orthotropic FGMs. The interaction integral proves to be an accurate and robust scheme in the

numerical examples where various types of material gradation, such as exponential, radial, and hyperbolic-tangent, are considered. We observe that material orthotropy, material gradation and the direction of material gradation (radial, Cartesian X_1, and Cartesian X_2) may have a significant influence on SIFs. We also observe that the crack tip location shows a significant influence on SIFs in hyperbolic-tangent materials. Moreover, the Poisson's ratio shows a negligible effect on SIF in a pure mode I problem, however, it may have a significant influence on SIFs in mixed-mode crack problems.

This work has contributed a method for evaluating SIFs in orthotropic FGMs by means of the interaction integral. Potential extensions of the present work involve prediction of crack initiation angles and crack propagation in brittle orthotropic FGMs. This is currently being pursued by the authors.

Acknowledgements

We gratefully acknowledge the support from NASA-Ames, Engineering for Complex Systems Program, and the NASA-Ames Chief Engineer (Dr. Tina Panontin) through grant NAG 2-1424. We also acknowledge additional support from the National Science Foundation (NSF) under grant CMS-0115954 (Mechanics & Materials Program). Any opinions expressed herein are those of the writers and do not necessarily reflect the views of the sponsors.

Appendix A. Derivatives of auxiliary strain fields

The auxiliary stress and displacement fields, Eqs. (7) and (8), are represented by complex variables. For the complex variables

$$\sqrt{z} = \sqrt{\cos\theta + \mu_k \sin\theta} = \sqrt{(\cos\theta + \alpha_k \sin\theta) + \mathrm{i}(\beta_k \sin\theta)} = \sqrt{x + \mathrm{i}y}, \tag{A.1}$$

where $\mathrm{i} = \sqrt{-1}$, the two solutions are possible:

$$\sqrt{z} = a + \mathrm{i}b \text{ and } \sqrt{z} = -(a + \mathrm{i}b). \tag{A.2}$$

The correct solutions for $\sqrt{z}$ are obtained such that the signs of displacements are satisfied. Thus for $K_{\mathrm{I}}^{\mathrm{aux}} > 0$ and $K_{\mathrm{II}}^{\mathrm{aux}} = 0$,

$$u_2^{\mathrm{aux}} > 0 \ (0 < \theta < +\pi), \quad u_2^{\mathrm{aux}} < 0 \ (-\pi < \theta < 0), \tag{A.3}$$

and for $K_{\mathrm{I}}^{\mathrm{aux}} = 0$ and $K_{\mathrm{II}}^{\mathrm{aux}} > 0$,

$$u_1^{\mathrm{aux}} > 0 \ (0 < \theta < +\pi), \quad u_1^{\mathrm{aux}} < 0 \ (-\pi < \theta < 0). \tag{A.4}$$

This approach extracts the expressions for the stresses and displacements involving real variables, which are originally expressed with the complex variables. The auxiliary stress fields are transformed to the global coordinates given by

$$\begin{aligned}
\sigma_{11}^{\mathrm{g}}(r,\theta) &= \cos^2\omega\sigma_{11}^{\ell}(r,\theta) + \sin^2\omega\sigma_{22}^{\ell}(r,\theta) - \sin(2\omega)\sigma_{12}^{\ell}(r,\theta),\\
\sigma_{22}^{\mathrm{g}}(r,\theta) &= \sin^2\omega\sigma_{11}^{\ell}(r,\theta) + \cos^2\omega\sigma_{22}^{\ell}(r,\theta) + \sin(2\omega)\sigma_{12}^{\ell}(r,\theta),\\
\sigma_{12}^{\mathrm{g}}(r,\theta) &= (\cos^2\omega - \sin^2\omega)\sigma_{12}^{\ell}(r,\theta) + \sin\omega\cos\omega(\sigma_{22}^{\ell}(r,\theta) - \sigma_{11}^{\ell}(r,\theta)),
\end{aligned} \tag{A.5}$$

where $(\cdot)^{\mathrm{g}}$ and $(\cdot)^{\ell}$ denote the global and local coordinates, respectively, and ω denotes the angle of the local coordinates with respect to the global coordinates, as shown in Fig. 2. The auxiliary strain fields, with respect to the global coordinates, are given by

$$\varepsilon_{ij}^{\mathrm{g}}(r,\theta) = S_{ijpq}(\boldsymbol{X})\sigma_{pq}^{\mathrm{g}}(r,\theta). \tag{A.6}$$

Thus the derivatives of the auxiliary strain fields can be evaluated as follows ($k = 1, 2$):

$$\varepsilon^{g}_{ij,k} = \frac{\partial \varepsilon^{g}_{ij}}{\partial X_k} = \frac{\partial \varepsilon^{g}_{ij}}{\partial r}\frac{\partial r}{\partial X_k} + \frac{\partial \varepsilon^{g}_{ij}}{\partial \theta}\frac{\partial \theta}{\partial X_k}, \tag{A.7}$$

where

$$\frac{\partial r}{\partial X_k} = \frac{\partial r}{\partial x_1}\frac{\partial x_1}{\partial X_k} + \frac{\partial r}{\partial x_2}\frac{\partial x_2}{\partial X_k} \tag{A.8}$$

and

$$\frac{\partial \theta}{\partial X_k} = \frac{\partial \theta}{\partial x_1}\frac{\partial x_1}{\partial X_k} + \frac{\partial \theta}{\partial x_2}\frac{\partial x_2}{\partial X_k}, \tag{A.9}$$

with

$$\frac{\partial r}{\partial x_1} = \cos\theta, \quad \frac{\partial r}{\partial x_2} = \sin\theta, \quad \frac{\partial \theta}{\partial x_1} = \frac{-\sin\theta}{r}, \quad \frac{\partial \theta}{\partial x_2} = \frac{\cos\theta}{r}. \tag{A.10}$$

References

Budiansky, B., Rice, J.R., 1973. Conservation laws and energy-release rates. Journal of Applied Mechanics, Transactions ASME 40 (1), 201–203.

Chang, J.H., Chien, A.J., 2002. Evaluation of *M*-integral for anisotropic elastic media with multiple defects. International Journal of Fracture 114 (3), 267–289.

Christensen, R.M., 1979. Mechanics of Composite Materials. John Wiley, New York.

Cook, R.D., Malkus, D.S., Plesha, M.E., Witt, R.J., 2002. Concepts and Applications of Finite Element Analysis, fourth ed. John Wiley & Sons Inc., New York.

Dolbow, J., Gosz, M., 2002. On the computation of mixed-mode stress intensity factors in functionally graded materials. International Journal of Solids and Structures 39 (9), 2557–2574.

Gu, P., Asaro, R.J., 1997. Cracks in functionally graded materials. International Journal of Solids and Structures 34 (1), 1–17.

Hirai, T., 1993. Functionally gradient materials and nanocomposites. In: Proceedings of the Second International Symposium on Functionally Gradient Materials. In: Holt, J.B., Koizumi, M., Hirai, T., Munir, Z.A. (Eds.), Ceramic Transactions, vol. 34. The American Ceramic Society, Westerville, OH, pp. 11–20.

Kanninen, M.F., Popelar, C.H., 1985. Advanced Fracture Mechanics. Oxford University Press, New York.

Kaysser, W.A., Ilschner, B., 1995. FGM research activities in Europe. MRS Bulletin 20 (1), 22–26.

Kim, J.-H., Paulino, G.H., 2002a. Finite element evaluation of mixed-mode stress intensity factors in functionally graded materials. International Journal for Numerical Methods in Engineering 53 (8), 1903–1935.

Kim, J.-H., Paulino, G.H., 2002b. Isoparametric graded finite elements for nonhomogeneous isotropic and orthotropic materials. Journal of Applied Mechanics, Transactions ASME 69 (4), 502–514.

Kim, J.-H., Paulino, G.H., 2002c. Mixed-mode fracture of orthotropic functionally graded materials using finite elements and the modified crack closure method. Engineering Fracture Mechanics 69 (14–16), 1557–1586.

Kim, J.-H., Paulino, G.H., 2003a. Mixed-mode *J*-integral formulation and implementation using graded finite elements for fracture analysis of nonhomogeneous orthotropic materials. Mechanics of Materials 35 (1–2), 107–128.

Kim, J.-H., Paulino, G.H., 2003b. An accurate scheme for mixed-mode fracture analysis of functionally graded materials using the interaction integral and micromechanics models. International Journal for Numerical Methods in Engineering, in press.

Kim, J.-H., Paulino, G.H., 2003c. *T*-stress, mixed-mode stress intensity factors, and crack initiation angles in functionally graded materials: a unified approach using the interaction integral method. Computer Methods in Applied Mechanics and Engineering 192 (11–12), 1463–1494.

Kim, J.-H., Paulino, G.H., submitted for publication. Consistent formulations of the interaction integral method for functionally graded materials.

Knowles, J.K., Sternberg, E., 1972. On a class of conservation laws in linearized and finite elastostatics. Archive for Rational Mechanics and Analysis 44 (2), 187–211.

Krenk, S., 1979. On the elastic constants of plane orthotropic elasticity. Journal of Composite Materials 13, 108–116.
Lekhnitskii, S.G., 1968. Anisotropic Plates. Gordon and Breach Science Publishers, New York.
Muskhelishvili, N.I., 1953. Some Basic Problems of the Mathematical Theory of Elasticity. Noordhoff Ltd, Holland.
Ozturk, M., Erdogan, F., 1997. Mode I crack problem in an inhomogeneous orthotropic medium. International Journal of Engineering Science 35 (9), 869–883.
Ozturk, M., Erdogan, F., 1999. The mixed mode crack problem in an inhomogeneous orthotropic medium. International Journal of Fracture 98 (3–4), 243–261.
Paulino, G.H., Jin, Z.H., Dodds Jr., R.H., 2002. Failure of functionally graded materials. In: Karihaloo, B., Knauss, W.G. (Eds.), Comprehensive Structural Integrity, vol. 2. Elsevier Science. (Chapter 13).
Raju, I.S., Shivakumar, K.N., 1990. An equivalent domain integral method in the two-dimensional analysis of mixed mode crack problems. Engineering Fracture Mechanics 37 (4), 707–725.
Rao, B.N., Rahman, S., 2002. Mesh-free analysis of cracks in isotropic functionally graded materials. Engineering Fracture Mechanics 70 (1), 1–27.
Rice, J.R., 1968. Path-independent integral and the approximate analysis of strain concentration by notches and cracks. Journal of Applied Mechanics, Transactions ASME 35 (2), 379–386.
Sampath, S., Herman, H., Shimoda, N., Saito, T., 1995. Thermal spray processing of FGMs. MRS Bulletin 20 (1), 27–31.
Sih, G.C., Paris, P.C., Irwin, G.R., 1965. On cracks in rectilinearly anisotropic bodies. International Journal of Fracture Mechanics 1 (2), 189–203.
Wang, S.S., Corten, H.T., Yau, J.F., 1980. Mixed-mode crack analysis of rectilinear anisotropic solids using conservation laws of elasticity. International Journal of Fracture 16 (3), 247–259.
Wawrzynek, P.A., 1987. Interactive finite element analysis of fracture processes: an integrated approach. M.S. thesis, Cornell University.
Wawrzynek, P.A., Ingraffea, A.R., 1991. Discrete modeling of crack propagation: theoretical aspects and implementation issues in two and three dimensions. Report 91-5, School of Civil Engineering and Environmental Engineering, Cornell University.
Yau, J.F., 1979. Mixed-mode fracture analysis using a conservation integral. Ph.D. thesis, Department of Theoretical and Applied Mechanics, University of Illinois at Urbana-Champaign.
Yau, J.F., Wang, S.S., Corten, H.T., 1980. A mixed-mode crack analysis of isotropic solids using conservation laws of elasticity. Journal of Applied Mechanics, Transactions ASME 47 (2), 335–341.